ExxonMobil

Underground Injection Control – Class VI Permit Application for Hummingbird Carbon Storage Project Injection Wells No. 01, No. 02, No. 03, No. 04, and No. 05

SECTION 1 – SITE CHARACTERIZATION

Hummingbird Carbon Storage Project
Allen Parish, Louisiana
ExxonMobil Low Carbon Solutions Onshore Storage, LLC
March 2025

SECTION 1 – SITE CHARACTERIZATION

TABLE OF CONTENTS

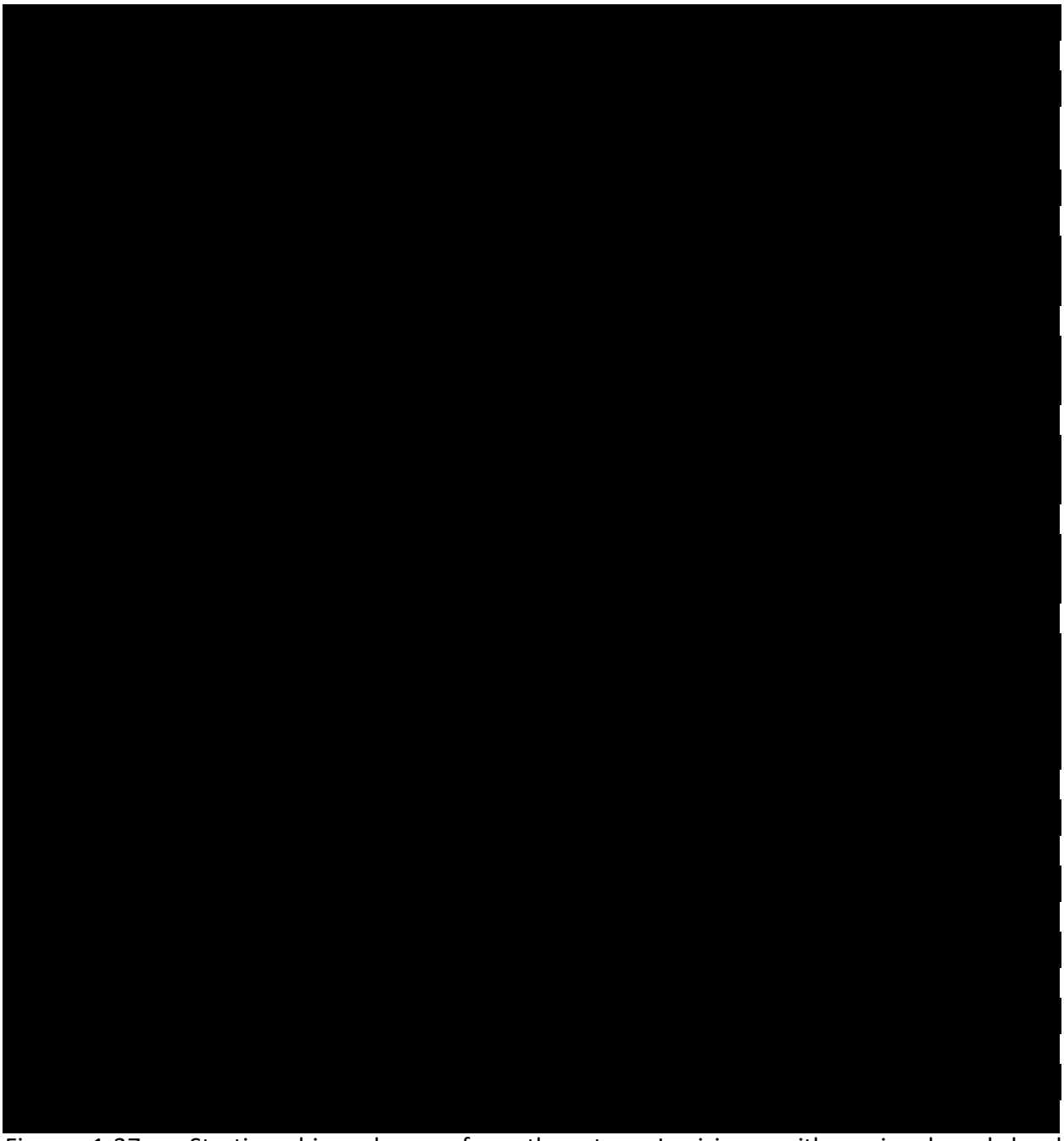

Tables

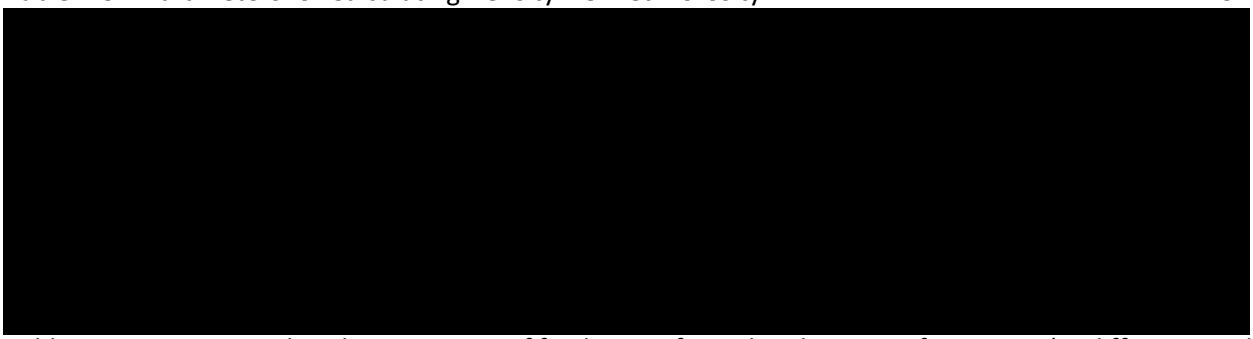

1.1 Overview

The site characterization for the Hummingbird Carbon Storage (CS) Project (Hummingbird Project) was prepared to meet the requirements of the Louisiana Administrative Code, Title 43 (LAC43): XVII **§3607.C.1.b**. ExxonMobil Low Carbon S [redacted] CO_2 will be sequestered over the life of the project. The purpose of this site characterization is to identify the potential risks and demonstrate, to the satisfaction of the Commissioner of Conservation (Commissioner), that the proposed site is suitable for the sequestration project. The key aspects of this demonstration are that the geologic formations provide adequate storage capacity to store the intended volume of injected CO_2, and that a competent confining zone is present that will contain the injected CO_2 throughout the life of the project.

ExxonMobil has completed a-review of site characterization data and analyses from multiple data types including public, proprietary, and licensed data sets. A high degree of confidence has been gained during this process regarding the effectiveness of the storage and confining properties of the sequestration site, and the anticipated alignment with data that will become available in the future.

1.1.1 Objectives

The following objectives were developed to demonstrate compliance with the requirements of SWO 29-N-6 **§3607**:

- Provide maps and cross sections of the area of review (AOR) (SWO 29-N-6 **§3607.C.1.b.ii** and **§3607.C.1.a**).
- Summarize available data on the depth, areal extent, thickness, mineralogy, porosity, permeability, and capillary pressure of the injection and confining zone(s) and on lithology and facies changes (SWO 29-N-6 **§3607.C.2.a**).
- Provide geologic and topographic maps and cross sections illustrating regional geology, hydrogeology, and the geologic structure of the local area (SWO 29-N-6 **§3607.C.1.b.i**).
- Identify the location, orientation, and properties of known or suspected faults and fractures that may transect the confining zone(s) in the AOR, along with an assessment that they will not interfere with containment (SWO 29-N-6 **§3607.C.1.b.iii**).
- Discuss the available geomechanical information on fractures, stress, ductility, rock strength, and in situ fluid pressures within the confining zone(s) (SWO 29-N-6 **§3607.C.2.b**).
- Present maps and stratigraphic cross sections indicating the general vertical and lateral limits of the underground sources of drinking water (USDWs) and water well completion details within the AOR, their positions relative to the injection zone, and the direction of water movement (where known) (SWO 29-N-6 **§3607.C.2.b.iv**).

- Summarize the available baseline geochemical data on subsurface formations, including the USDWs in the AOR (SWO 29-N-6 **§3607.C.2.e**).
- Summarize the available information on the seismic history of the area, including the presence and depths of seismic sources, and an assessment of the potential for seismicity to interfere with containment (SWO 29-N-6 **§3607.C.2.c**).

1.2 Regional Geology

Tectonostratigraphic and Paleoclimatic History – Northern Portion of the Gulf of Mexico Basin

The incipient Gulf of Mexico basin (Figure 1-1) formed through the extension of largely continental crust during the Late Triassic to Early Jurassic breakup of the Pangean supercontinent, specifically rifting between the North American and South American plates (Bird et al., 2005 and references therein; Galloway, 2008). Rifting and basin growth accelerated into the Late Jurassic and Early Cretaceous (Salvador, 1987; Jacques and Clegg, 2002; Galloway, 2008). As a result, areas immediately outside the basin consist of unmodified continental crust, while the basin itself is underlain by shallow (2–12 kilometers deep), moderately thinned, transitional crust along the margin—and progressively more extended, thinner, and deeper (up to 20 kilometers) transitional crust to marine crust near the basin center (Galloway, 2008). Crustal extension prior to this accelerated growth phase ultimately resulted in a structural sag on the western side of the basin.

All figures here in *Section 1.2* are displayed in high resolution in *Appendix B-1***.**

This structural low allowed Pacific Ocean water to enter the basin—a connection that was fully established by the Middle to Late Callovian. Deposition within the basin switched from primarily terrestrial facies to a hypersaline, restricted-marine facies (Galloway, 2008). This switch is recorded by the widespread deposition of evaporitic deposits, collectively referred to as the Louann Salt. The abrupt transition from older, synrift continental deposits to more widespread, marine-influenced evaporitic deposits is commonly used to define the base of the Gulf of Mexico basin fill succession (Sawyer, 1991; Galloway, 2008).

Accelerated extension caused by Callovian-age crustal rupture, emplacement of basaltic crust, and increased seafloor spreading rates resulted in the termination of widespread evaporitic deposition in the basin. By the end of the Early Cretaceous, spreading centers had shifted east into the Atlantic and Caribbean basins. As a result, the crust underpinning the Gulf of Mexico basin began to cool and subside.

A series of basin-rimming Aptian-Albian carbonate platforms (i.e., Sligo Formation, James Limestone, Rodessa Formation, and Glen Rose Limestone, to name a few) developed on the more slowly subsiding basin margin (Winker and Buffler, 1988). Clastic sediments were largely constrained to an area inboard of the platform carbonates along the periphery of the basin. It was at that time that the Gulf of Mexico achieved its current morphologic form. These carbonate platforms ultimately drowned in the Late Cretaceous due to high, load-driven subsidence rates. By the start of the Cenozoic, clastic depositional systems previously constrained to the basin margin begin to prograde and fill the basin—and this process continues through today (Figure 1-2).

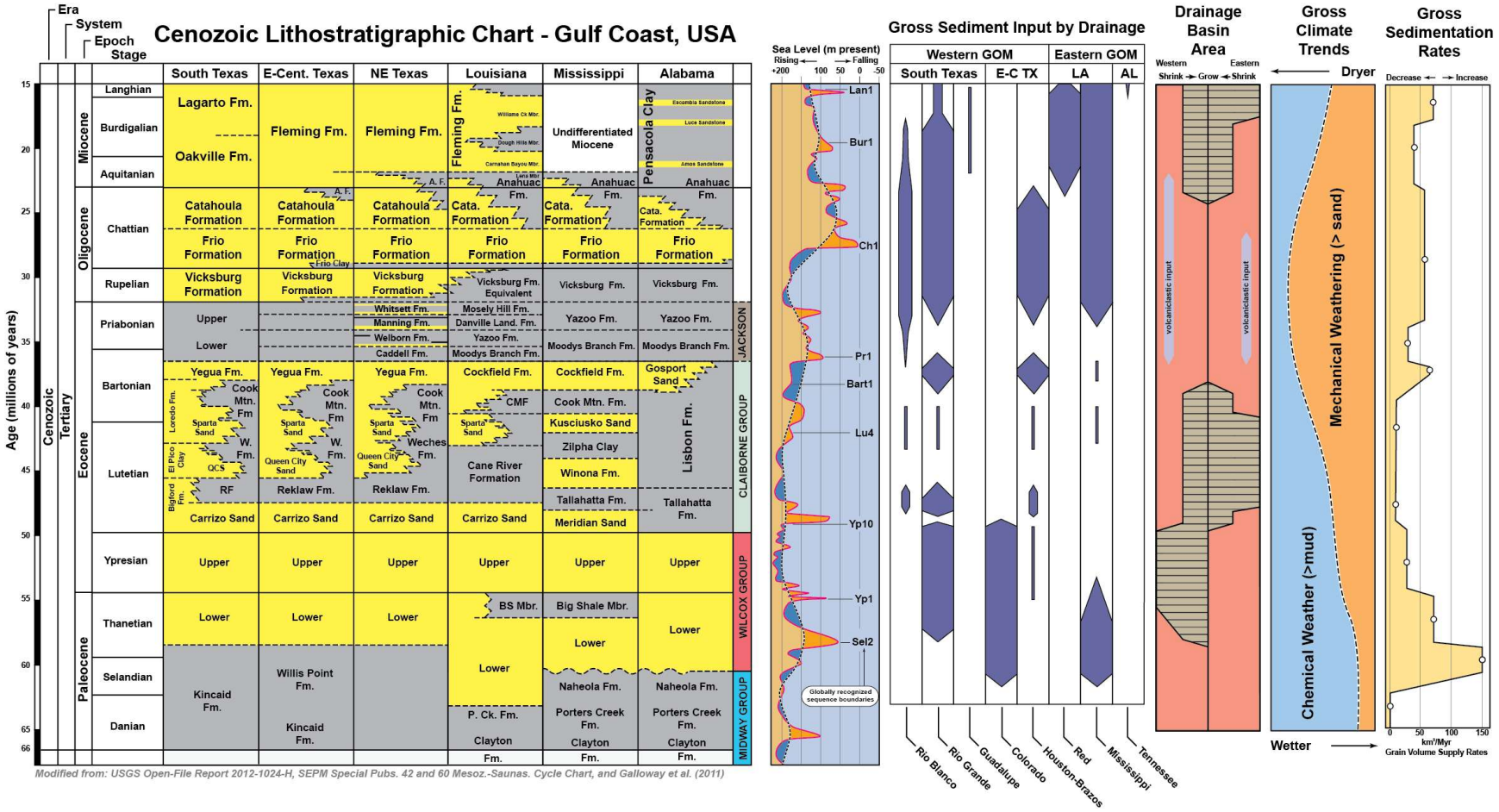

Figure 1-2 – Lithostratigraphic correlation chart for the northern portion of the Gulf of Mexico basin (left). Yellow formations represent more sandy intervals, and gray formations represent more muddy intervals. A comparison of stratigraphic forcing mechanisms, relative to the development of formations within the basin, are shown to the right.

Paleoclimates, Eustasy, and Fluvial Drainage Area Evolution – Greater Gulf of Mexico Region

The Cenozoic fill succession records the climatically modulated delivery of sediment from the interior of the continental United States to the Gulf of Mexico basin. Although long-term climatic trends played an important role in the style, scale, and sediment flux of fluvial delivery systems to the Gulf of Mexico basin, far-field tectonic influences and modification of the paleo-landscape played an equally important role in the development and evolution of catchment areas and drainage-basin networks (Figure 1-3). As sediment was delivered to the basin margin, eustasy and relative sea level had a profound influence on the location and style of deposition, depositional body morphology, and stratal stacking patterns within the coastal to fully marine portions of the receiving basin.

Galloway et al. (2011) provided a detailed description of Cenozoic forcing mechanisms, their variability through time across the continental interior and Gulf Coast regions of the United States, and maps of drainage basin evolution. Figure 1-2 summarizes observations from Galloway et al. (2011) concerning sediment supply to the major Gulf of Mexico depocenters through the Cenozoic. This figure also illustrates the timing and location of key sequence stratigraphic surfaces, long-term stratal stacking trends, and the development of reservoir-seal couplets in the basin.

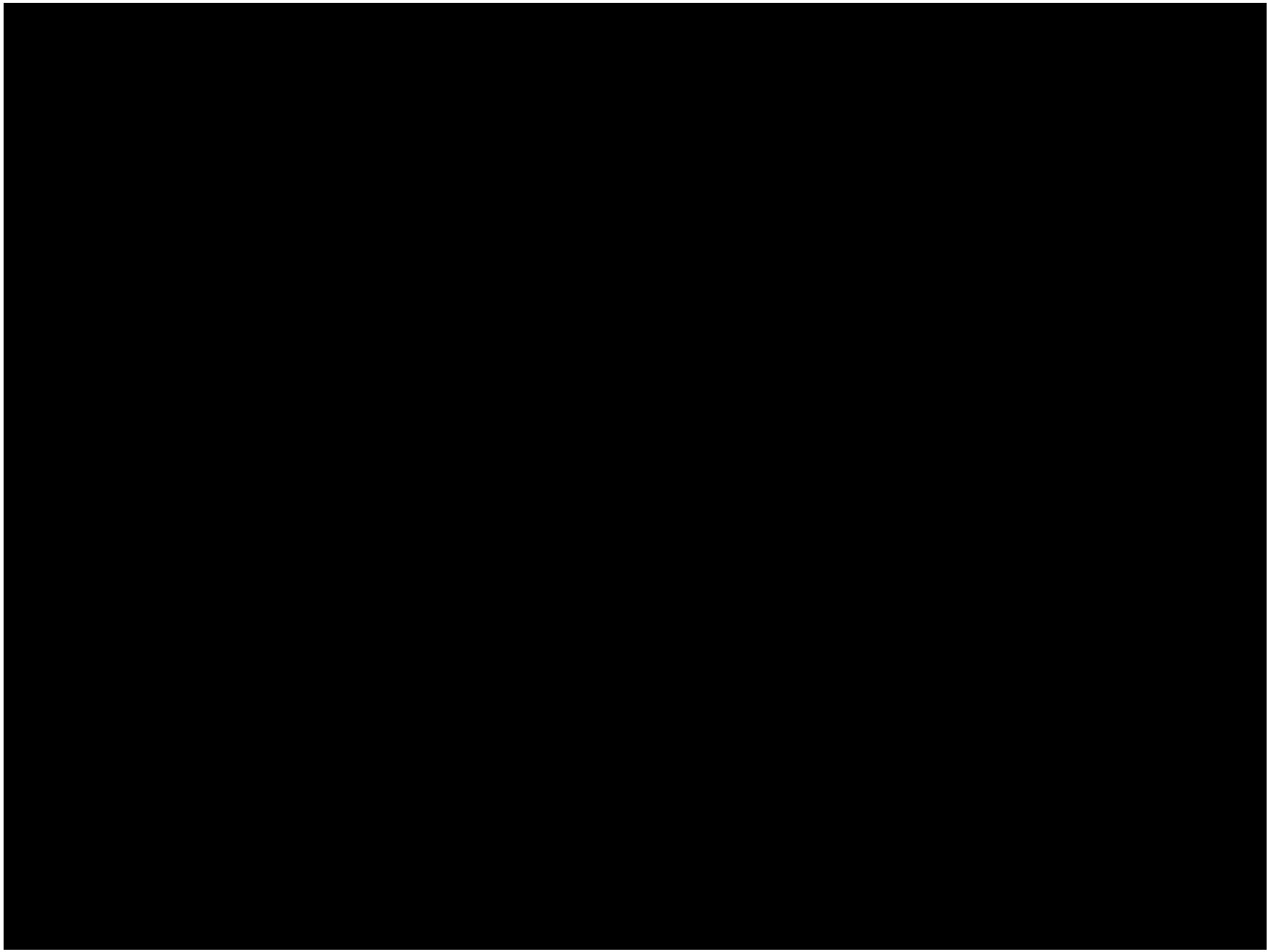

Northern Gulf of Mexico Basin Cenozoic Fill Succession

The Cenozoic fill succession is characterized by a largely progradational stack of both ramp-style and passive margin-style continental shelves (Figures 1-4 through 1-6). The overall pattern of south-directed progradation reflects, in part, the load-driven generation of accommodation due to the overall deepening of the Gulf of Mexico basin. Loading also played a major role in the deformation of the northern Gulf of Mexico. Observed deformation can be separated into three different but interrelated styles: (1) extensional faulting and failure of the distal portions of coastal prisms and/or continental shelf edges along large, down-to-the-south, mostly listric faults; (2) Louann Salt migration associated with differential loading and development of salt diapirs, stocks, canopies, welds, and salt evacuation mini-basins; and (3) far-field tectonic effects associated with Laramide thrusting events in the western interior of the continental United States.

Figure 1-2 summarized many of the key forcing mechanisms that influenced the deposition of major reservoir and seal systems across much of the basin. [redacted]

[redacted] The observed reservoir types, qualities, thicknesses, and connectivity change across the zone are strongly influenced by proximity to drainage basin outlets (depocenter); hinterland mineralogy and timing of sediment delivery to the coast; coastal marine processes at and between primary depocenters; local tectonics; and the position and direction of the sea-level fluctuations through [redacted] form a southward prograding coastal prism consisting of fully marine, marine-influenced fluvial, fluvial, and coastal plain deposits. The form of this coastal prism was modified by extensional faulting and salt-related folding and by younger faulting, but reconstructions indicate [redacted] had a typical, passive margin-type shape—and that the youngest shelf-slope break parallels the modern-day shoreline along the Texas sector of the Gulf Coast (Figure 1-3).

[redacted] Major depocenters at the mouth of the Houston-Brazos system in eastern Texas and the Mississippi system in central Louisiana were receiving significant volumes of sediment at this time (Galloway et al., 2011). In the Hummingbird Project area, a large, river-dominated deltaic complex (referred to herein as the Mississippi delta) with attached wave-dominated strandplains formed (Figure 1-3).

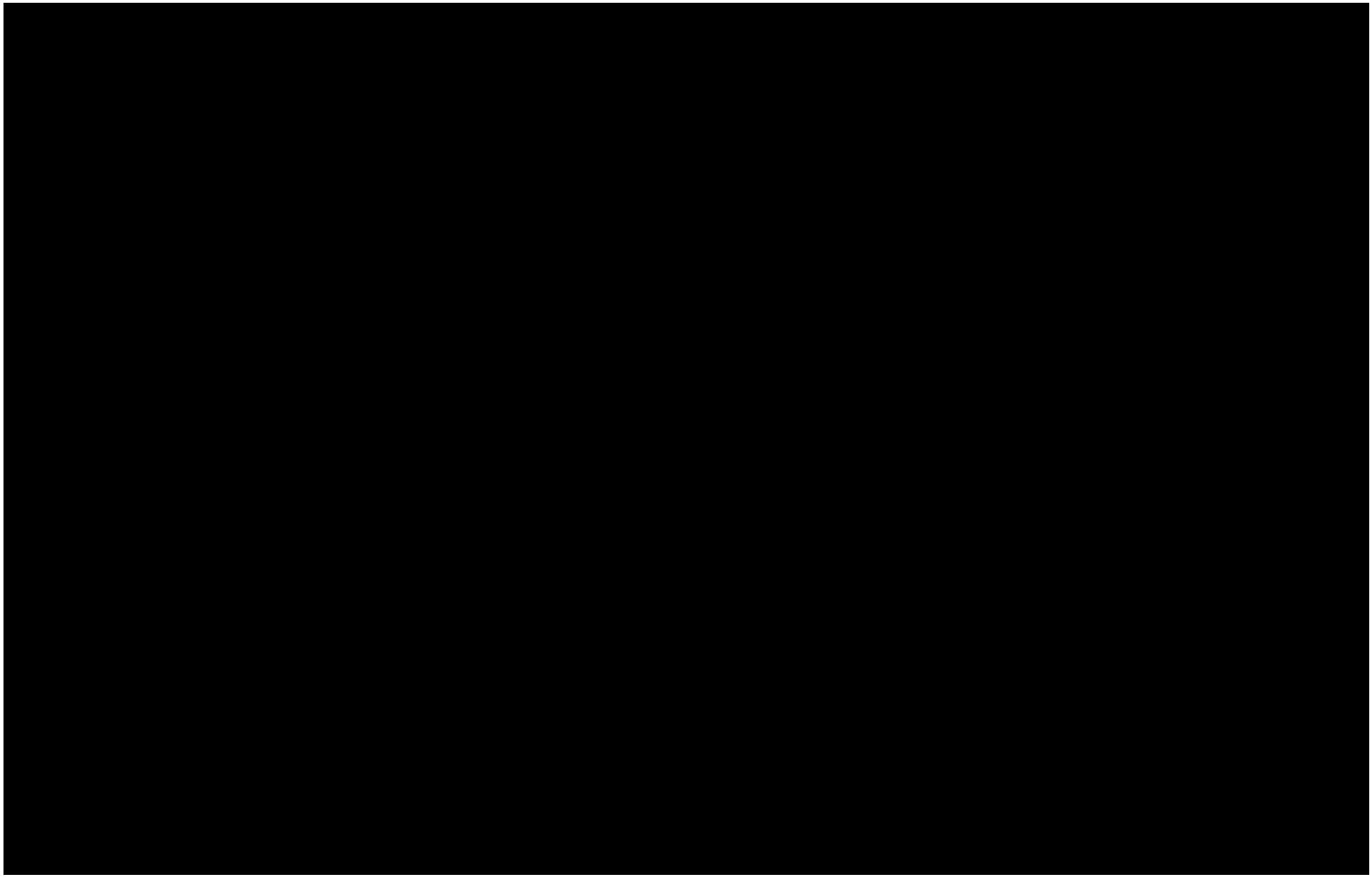

[redacted] As a result, surface gradients [redacted] were relatively steep in the hinterland, and fluvial systems likely became more efficient at delivering sediment to the Gulf of Mexico basin. Arid climatic conditions dominated [redacted]. Therefore, mechanical weathering outpaced chemical weathering in the hinterland, generating an overabundance of reservoir-grade sands that could be delivered to the Mississippi delta.

Records of global sea-level fluctuations (Figure 1-2) indicate that the position of sea level was significantly higher [redacted]. This overall trend from relatively high to substantially lower sea-level positions in the Gulf of Mexico is reflected in the stratal stacking patterns and lithologic assemblages in the basin, indicating that eustatic effects played a major role in the spatial and temporal position of shorelines and key reservoirs, and the development of internal and ultimate sealing intervals within [redacted]. Figure 1-2 illustrated the observed stratal architecture for the [redacted] in the eastern Texas and western Louisiana sectors of the Gulf of Mexico basin, [redacted]

[redacted]

[redacted]

[redacted]

1.3 Site Geology

The AOR, located in Allen Parish, Louisiana (Figure 1-8), is defined by the combination of the maximum critical pressure front and stabilized CO_2 plume for all intervals. Geological properties and characterization of the injection and confining zones within the AOR are drawn from proprietary, licensed, subscribed, and public data sources. [redacted]

Data from existing wells in Allen Parish, published literature, and publicly available datasets including the Louisiana Department of Energy and Natural Resources (LDENR) and the Louisiana Geological Survey (LGS), IHS LogNet, Enverus, Core Laboratories' Reservoirs Applied Petrophysical Integrated Data (RAPID) service were used to characterize the subsurface. General geologic setting and lithological attributes are described regionally from publications and offset well log data in the project area. [redacted] A seismic cross section through the proposed Hummingbird Injection Well (INJ) No. 01, No. 02, No. 03, No. 04, and No. 05 is shown in Figure 1-9. Key stratigraphic layers are described in this section, while faults and fault seal properties are described in *Section 1.5*.

[redacted]

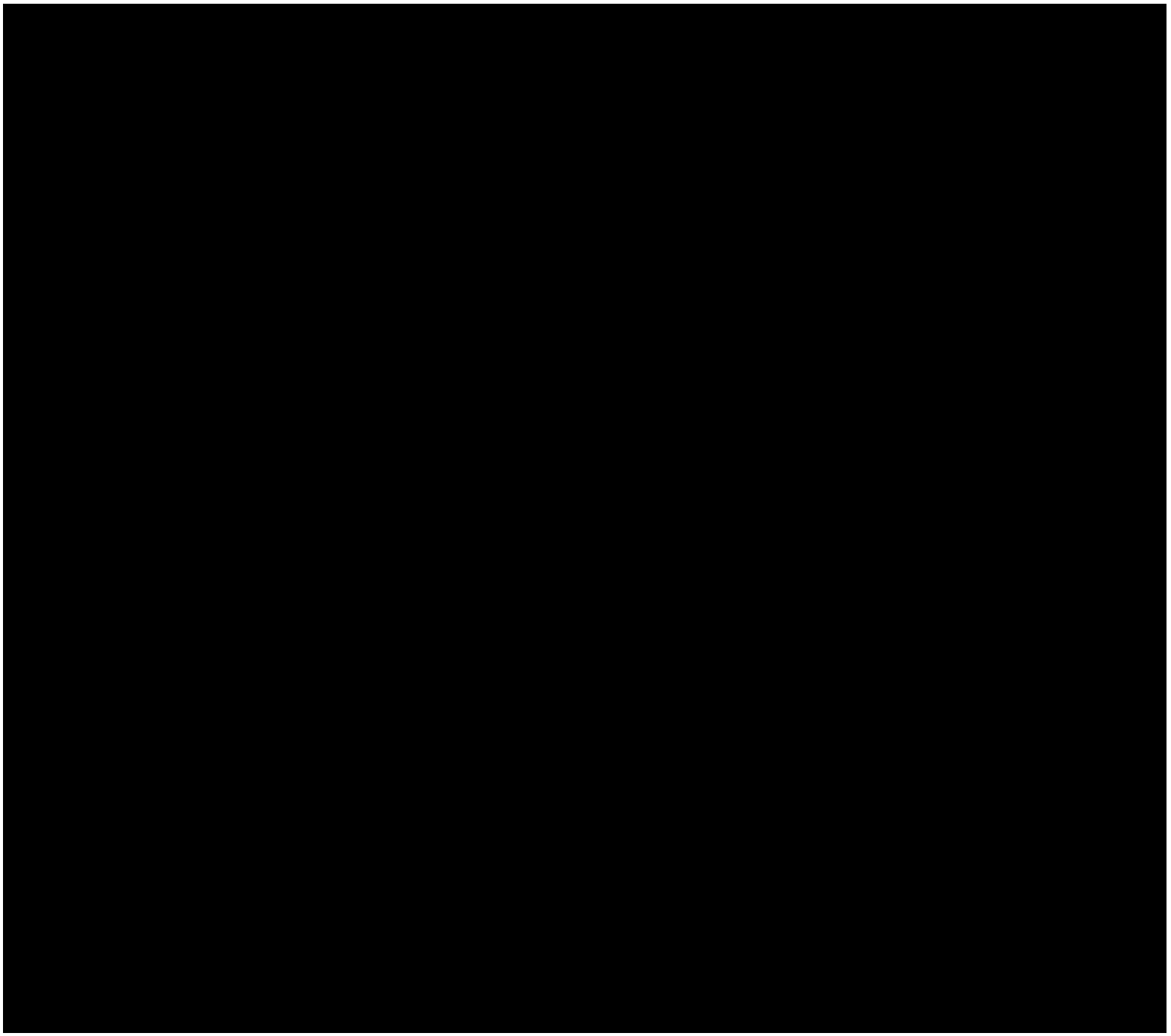

[redacted]

[redacted]

*MD – measured depth

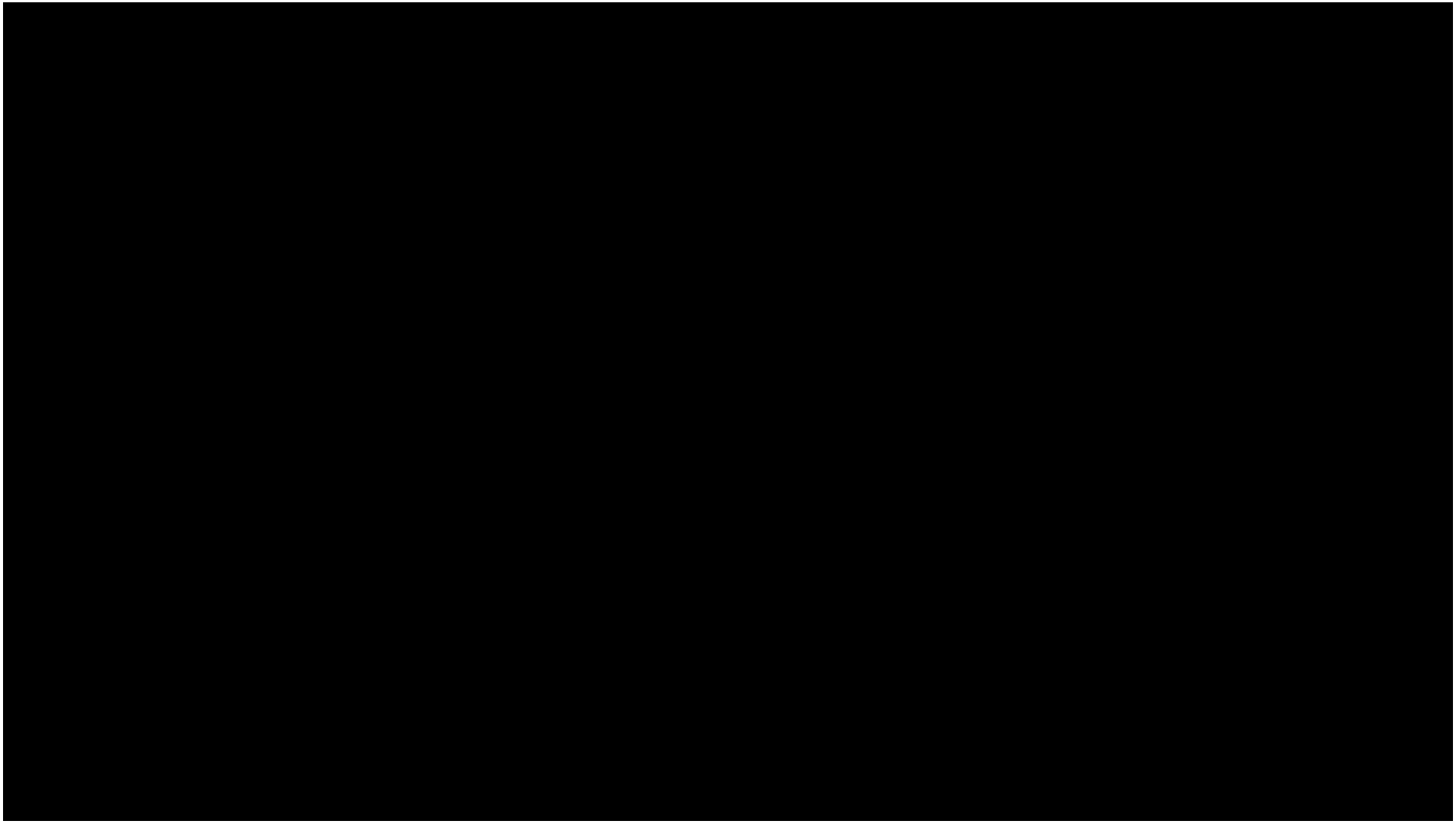

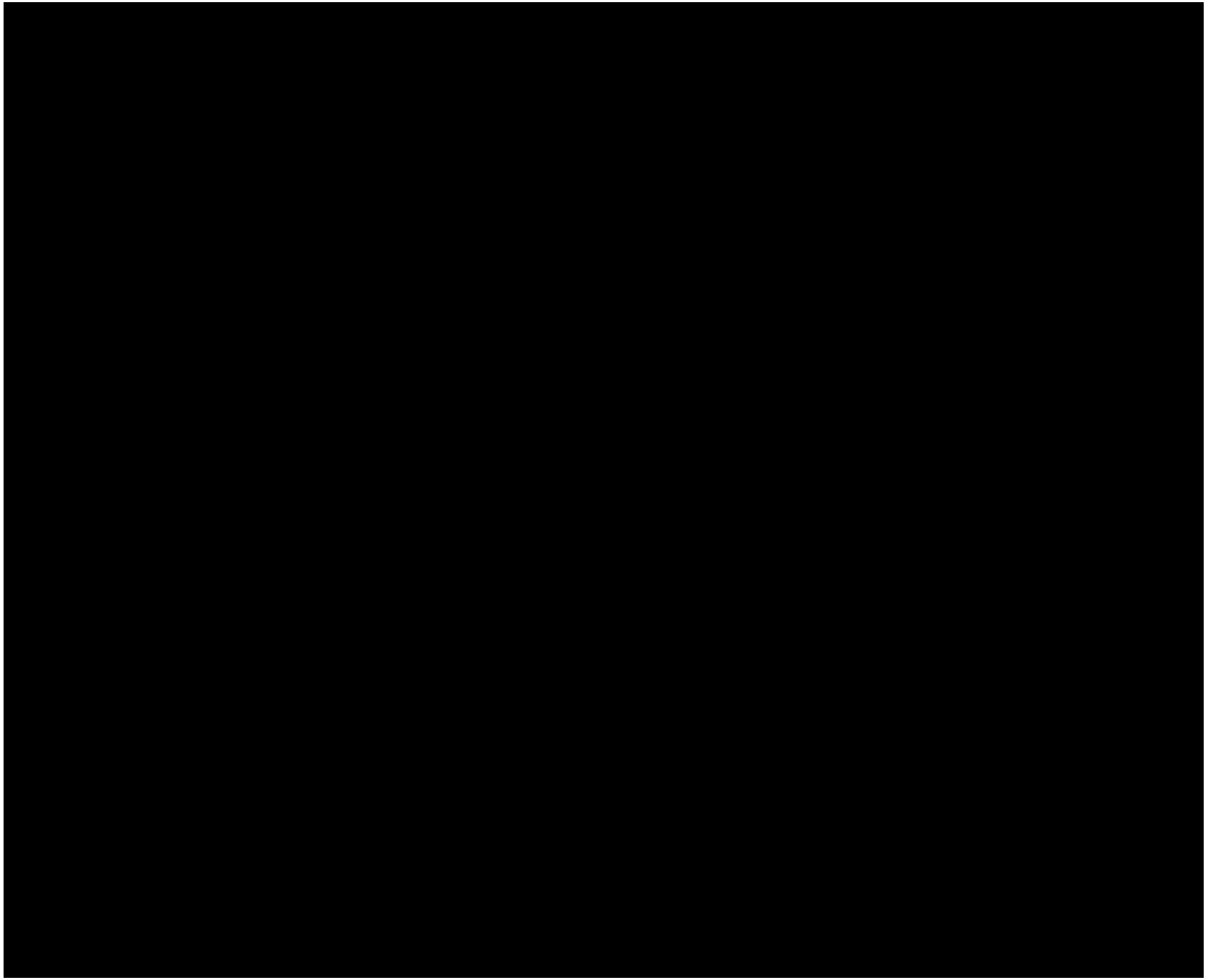

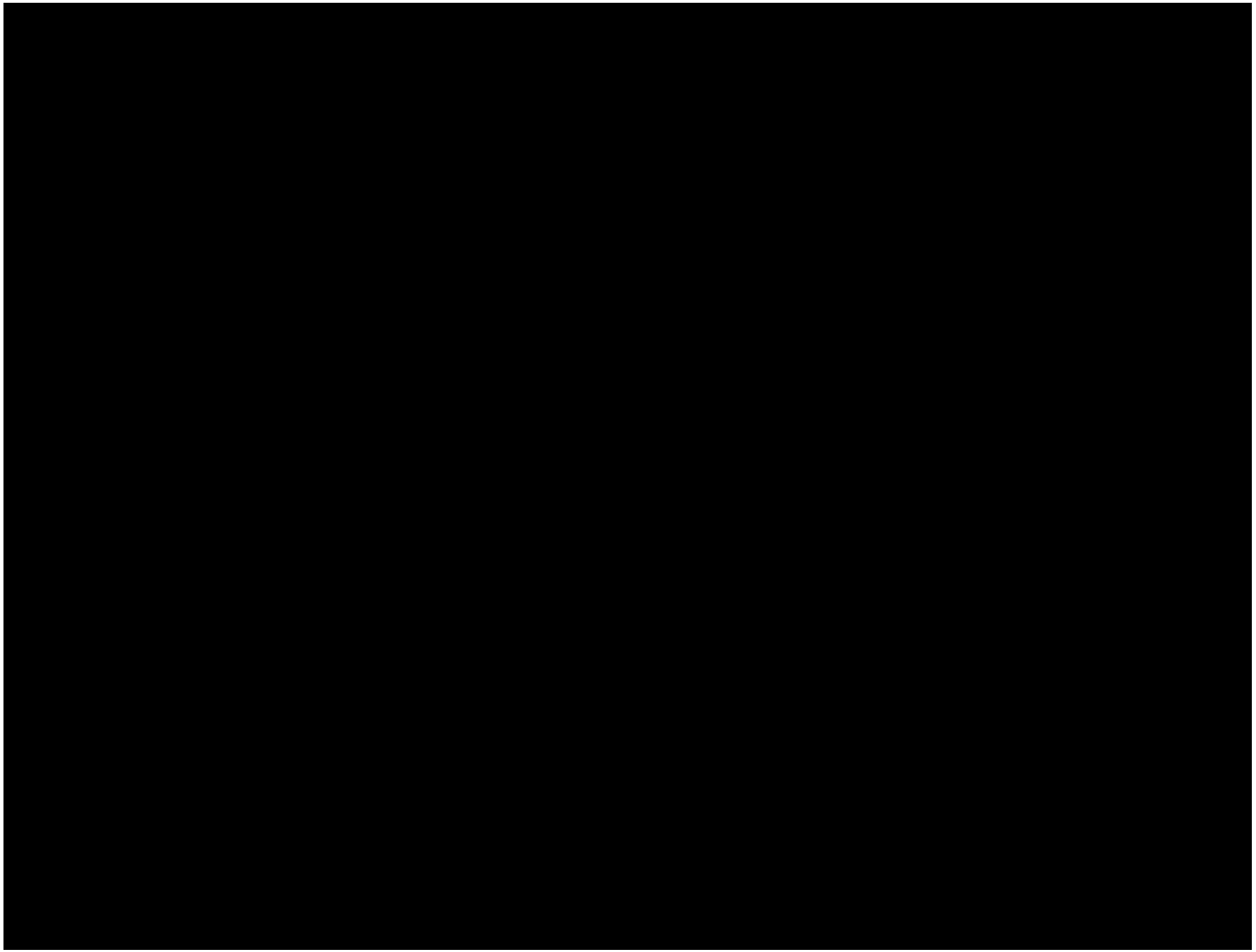

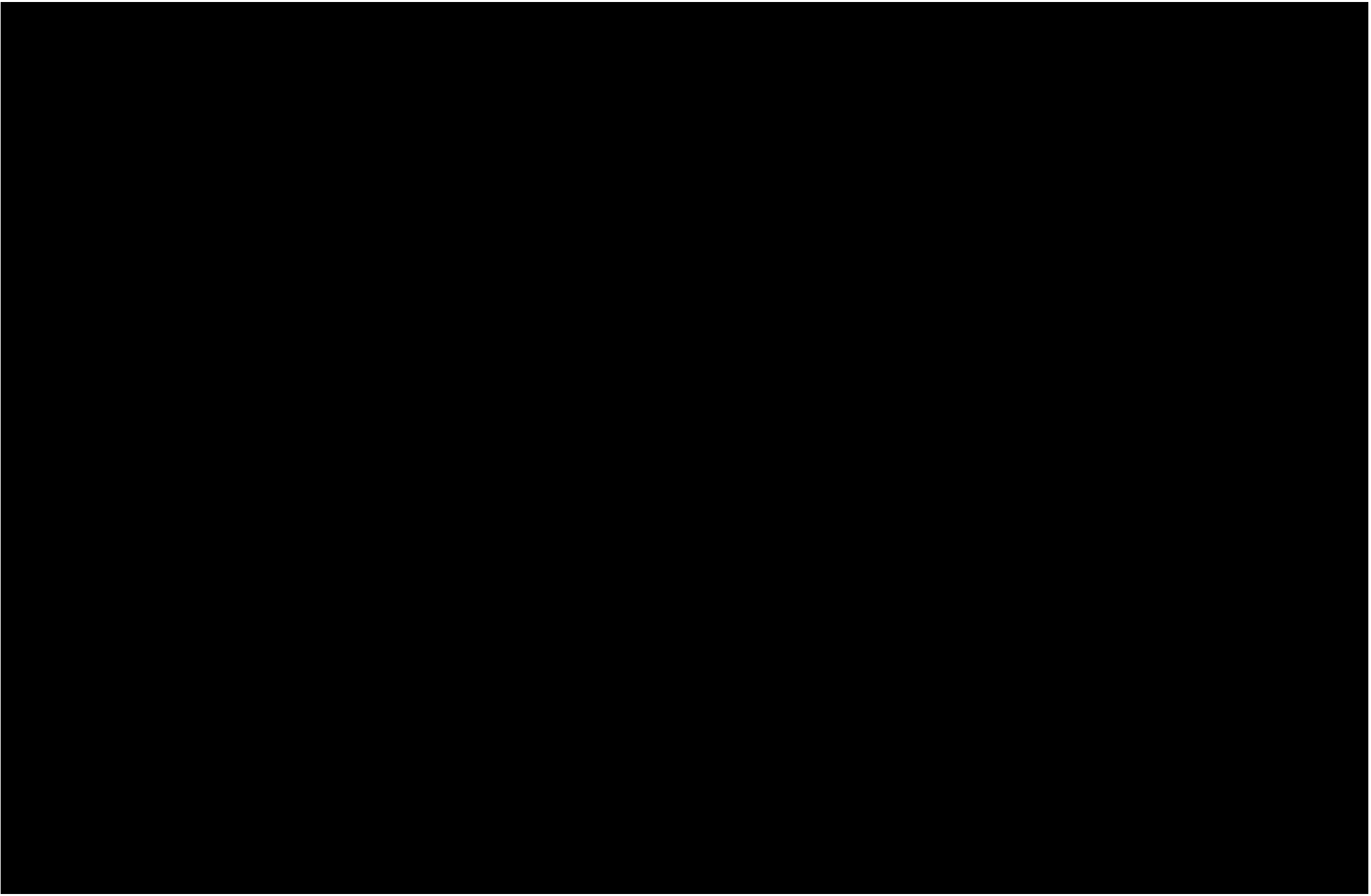

1.3.1 Injection Zone

The injection zone is composed of the [redacted] The different injection intervals are separated by a mix of regionally extensive shales, and more locally extensive intraformational shale. Depth structure maps and thickness maps for the injection intervals are shown in Figures 1-13 and 1-14, respectively. Because of the well density and compressed scale of the maps in these figures, [redacted]) showing well locations relative to the AOR.

[redacted] targeted for injection are composed of interbedded sandstones, siltstones, and shales sourced primarily from the [redacted] within the project area contains primarily prograding to downstepping fluvially dominated deltaic complexes and attached shorefaces. [redacted] In the following sections, all gross formation thicknesses are given as (mean ± one standard deviation).

[redacted]

[redacted]

[redacted]

[redacted]

1.3.2 Confining System

The confining system for the Hummingbird Project protects the USDW and is comprised of a primary UCZ and multiple deeper, redundant intraformational seals separating injection intervals from each other. Key containment intervals are the UCZ, [redacted] provides a table ([redacted] with pertinent well

information and a detailed map [redacted] showing well locations relative to the AOR for all wells used to generate the thickness maps.

[redacted]

[redacted]

[redacted]

[redacted]

1.4 Porosity

1.4.1 Well Data

Petrophysical evaluations were performed on [redacted] wells to estimate shale volume (VSH) and total porosity (PHIT) from wireline logs across the [redacted]. For the [redacted] wells evaluated, all wells had either an SP or gamma ray (GR) log to estimate shale volume. Of these [redacted] wells, [redacted] had either a compressional sonic (DTC) and/or bulk density (RHOB) log to estimate total porosity across the formations of interest. Table [redacted] in [redacted] lists the wells and log data, including neutron porosity (NPHI), available for analysis.

1.4.2 Log Quality Control

Many legacy wells were affected by poor borehole conditions, therefore additional steps were required to ensure consistent petrophysical properties between the wells. These steps are discussed in greater detail in the following section.

1.4.3 Methodology

1.4.3.1 Shale Volume (VSH)

Shale volume was primarily determined from the SP log. The SP logs were baselined in thick shales to read zero millivolts (mV), and clean sand values were interpreted for each well based on the magnitude of the SP deflection. Shale volume was then calculated from the SP log as follows in Equation 1:

(Eq. 1)

$$VSH\_SP = \left\lfloor \frac{SP_{log} - SP_{clean}}{SP_{sha} - SP_{clean}} \right\rfloor$$

In the absence of an available SP log, the GR log was used to calculate shale volume. Similar to the SP approach, the GR logs were bulk-shifted to read approximately 100 GAPI in shales, and clean sand values were interpreted for each well. Shale volume was then calculated from the GR log as follows in Equation 2:

(Eq. 2)

$$VSH\_GR = \left\lfloor \frac{GR_{log} - GR_{clean}}{GR_{shale} - GR_{clean}} \right\rfloor$$

1.4.3.2 Total Porosity

Compressional sonic was the most common porosity log available. To compute total porosity, the method proposed by Raymer et al. (1980) was used. This method is particularly well-suited for high-porosity, unconsolidated sands typical of the Gulf Coast region. Additionally, a "Shale Reduced" option was selected to correct the high apparent porosities related to increasing shale content (i.e., due to an increase in measured slowness). Total porosity from the sonic logs was calculated as follows in Equation 3:

(Eq. 3)

$$DT_{SR} = \text{maximum}\left[DT_{ma}, \left(\frac{DT_{log} - V_{sh} * DT_{sh}}{1 - V_{sh}}\right)\right]$$

$$\emptyset_S = \left[C * \left(\frac{DT_{SR} - DT_{ma}}{DT_{SR}}\right) * (1 - V_{sh})\right] + (V_{sh} * \emptyset_{sh})$$

where DT_{SR} is the shale-reduced slowness, DT_{sh} is the measured shale slowness from sonic logs, Φ_S is the sonic-derived total porosity, and Φ_{sh} is shale porosity (assumed or known a priori). Table 1-2 provides the parameters used for calculating sonic-derived porosity.

Table 1-2 – Parameters for Calculating Sonic-Derived Porosity

Parameter	Value or Function
Compaction Factor, *C*	[redacted]
Matrix Slowness, DT_{ma}	55.5 µs/ft (default for sandstones)
Shale Slowness, DT_{sh}	10 ^ (2.205 - 0.0000285 * DEPTH + 0.000000001 * DEPTH^2)
Shale Porosity, $\emptyset_{sh}$	0.15

*µs/ft – microseconds per foot

Bulk density logs were used to estimate total porosity in six additional wells. In general, estimating porosity from bulk density logs is more straightforward since any increase in shale content typically results in a higher measured bulk density (or lower apparent porosity). However, as noted previously, many legacy wells were affected by borehole washouts, which adversely impacts the bulk density measurement. Consequently, a similar approach using shale volume was implemented where density-derived porosity was calculated as follows in Equation 4:

(Eq. 4)

$$\emptyset_D = (1 - V_{sh}) * \left(\frac{\rho_{ma} - \rho_{log}}{\rho_{ma} - \rho_f}\right) + V_{sh} * \theta_{sh}$$

where Φ_D is the density-derived total porosity, ρ_{ma} is the matrix density, and ρ_f is the fluid density. Table 1-3 provides the parameters used for calculating density-derived porosity. A total porosity ($\emptyset_T$) equation follows in Equation 5.

Table 1-3 – Parameters for Calculating Density-Derived Porosity

Parameter	Value
Matrix Density, ρ_{ma}	2.65 g/cm^3 (default for sandstones)
Fluid Density, ρ_f	1 g/cm^3
Shale Porosity, ϕ_{sh}	0.15

*g/cm^3 – grams per cubic centimeter

(Eq. 5)

$$\emptyset_T = \frac{(\emptyset_D + \emptyset_{RES})}{2} \; or \; \emptyset_T = \frac{(\emptyset_S + \emptyset_{RES})}{2}$$

where ϕ_{RES} is the conductivity-derived porosity.

[redacted]

1.5 Geologic Structure

Regional dips are [redacted] and vary on average between [redacted] within the AOR (Figure 1-17). [redacted]

[redacted]

1.5.1 Seismic Survey Data

[redacted]

[redacted]

1.5.1.1 Velocity Control and Synthetic Seismogram

The wells that contained enough data to perform a well tie (i.e., tie the seismic survey to depth and allow the correlation of historical well logs to seismic data) in proximity to the Hummingbird Project [redacted] The map in Figure 1-18 shows the location of these wells relative to the project AOR. [redacted] The results of the well ties are shown in Figures 1-19 through 1-22.

Time-depth relationships were generated from the respective sonic logs, and all [redacted] offered good ties for the purposes of geologic characterization at the project site. High-quality well ties, as discussed in this section, yield a good conversion of the seismic data from time to depth, allowing for a quality comparison between well data and seismic data. In areas without well control, a regional velocity model was utilized—built from a network of regional 2D seismic data, which generally yielded decent time-depth conversion results as blind-tested at the well locations.

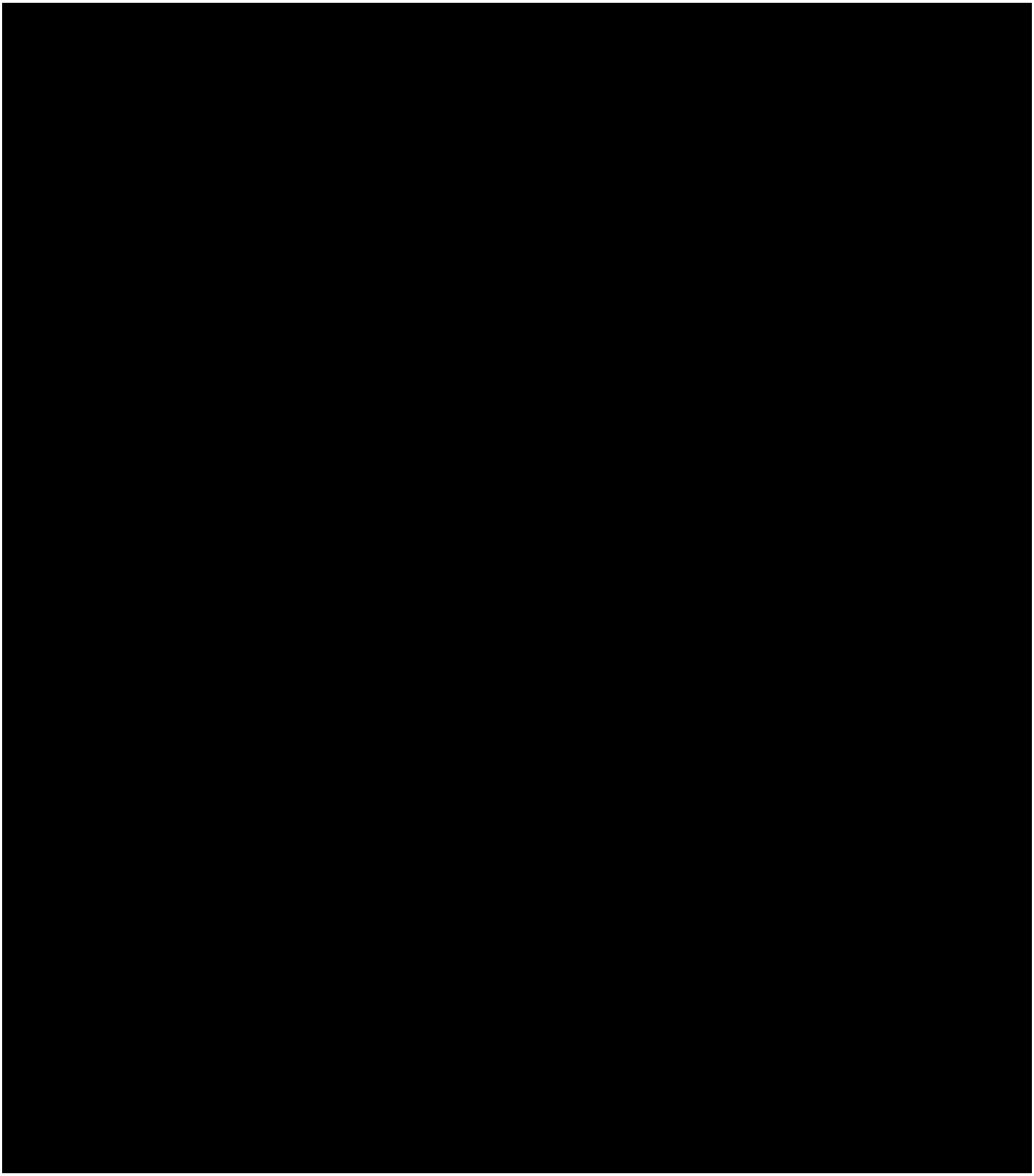

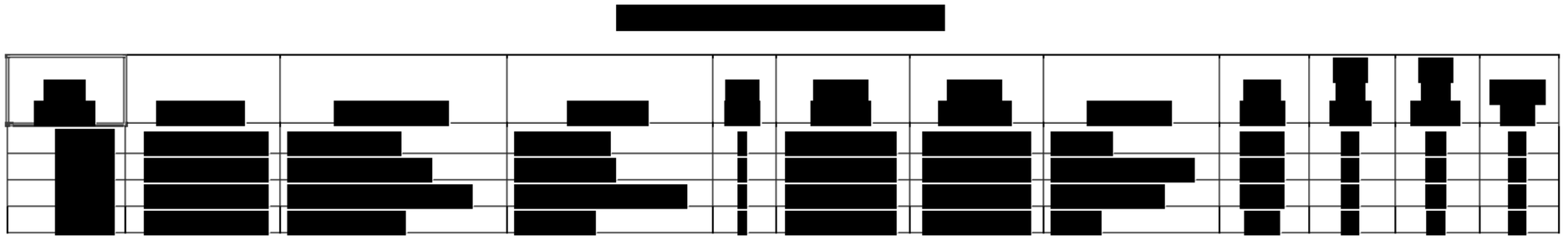

*OG – oil and gas
O – oil
KB – kelly bushing

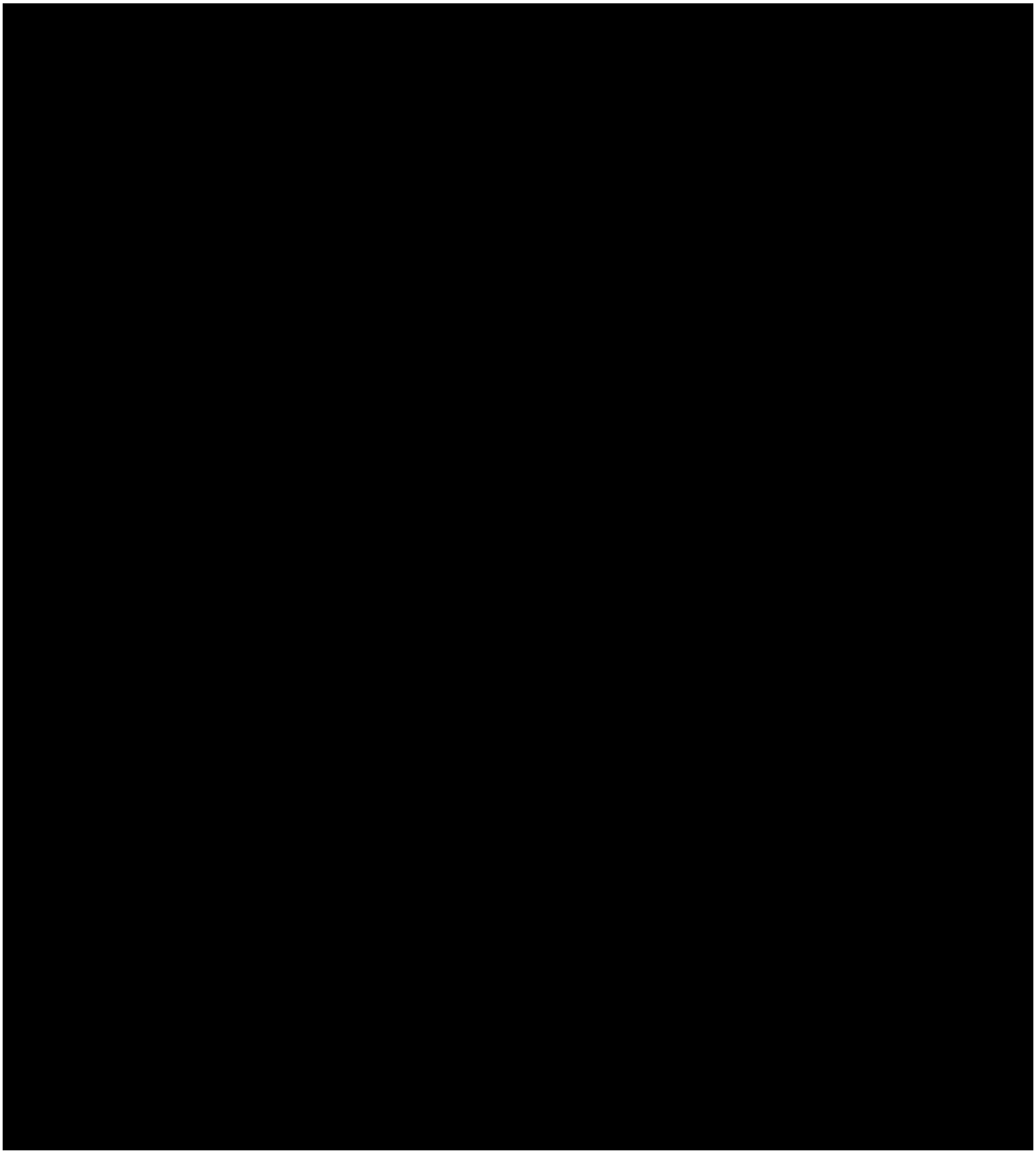

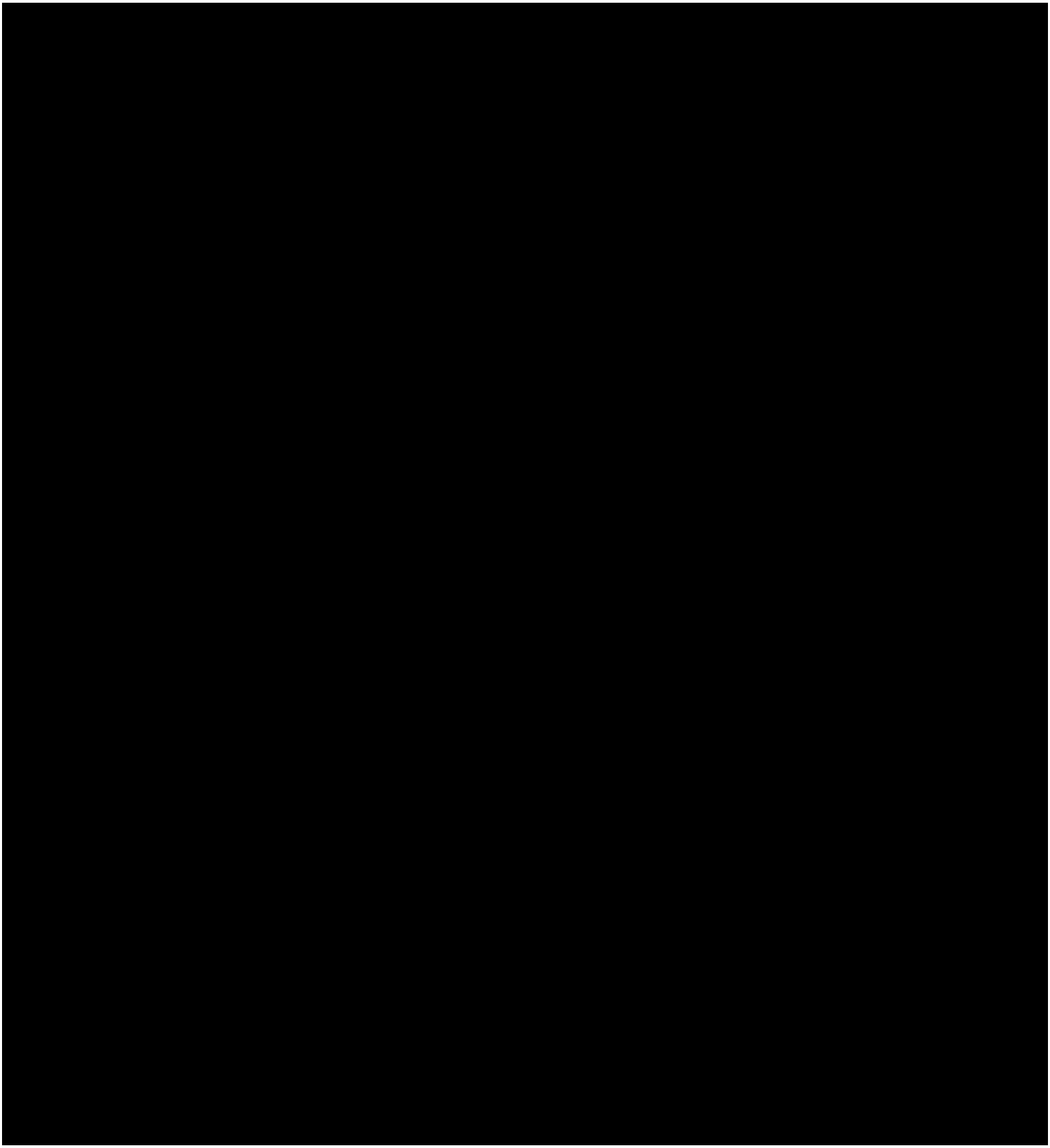

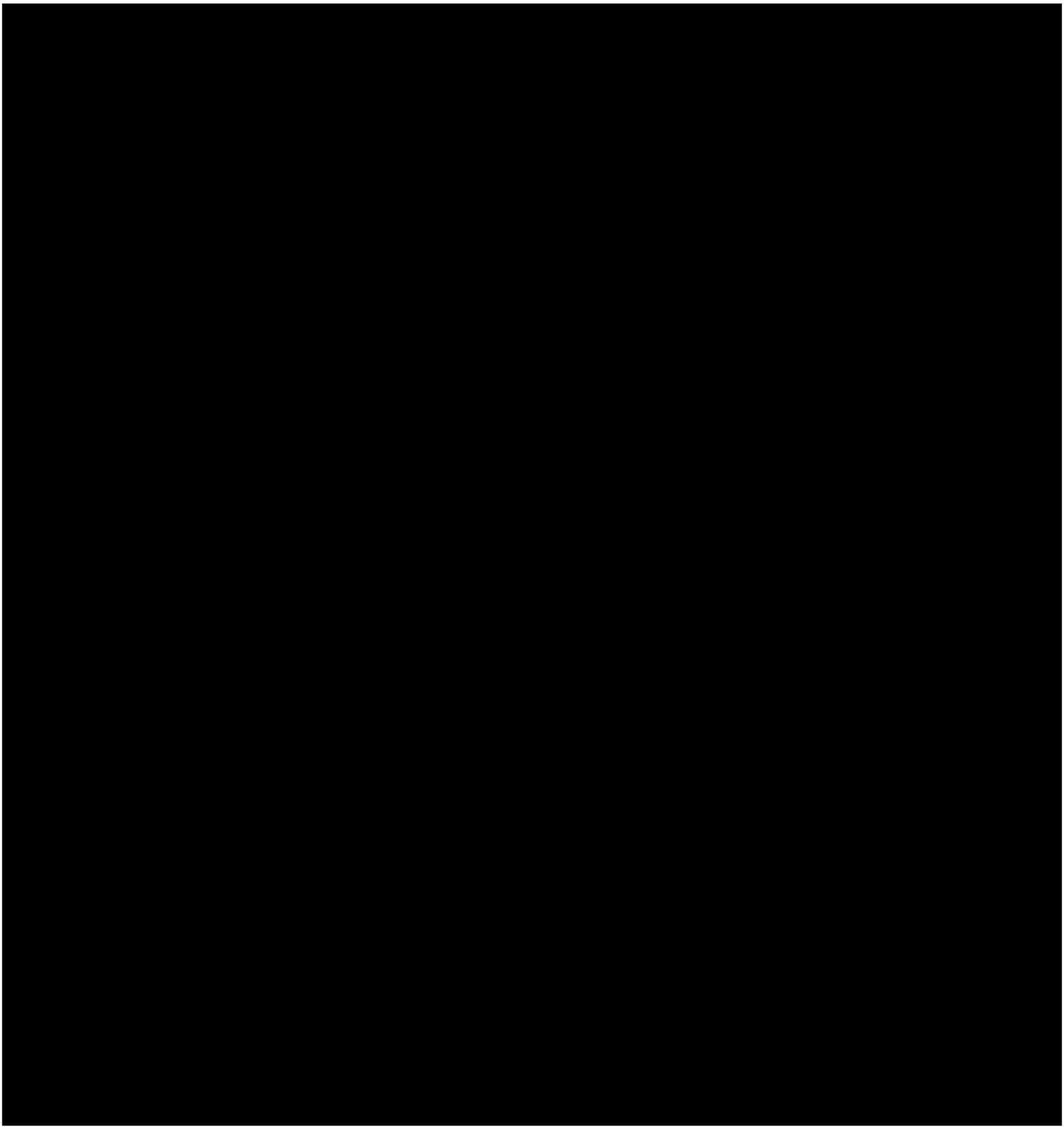

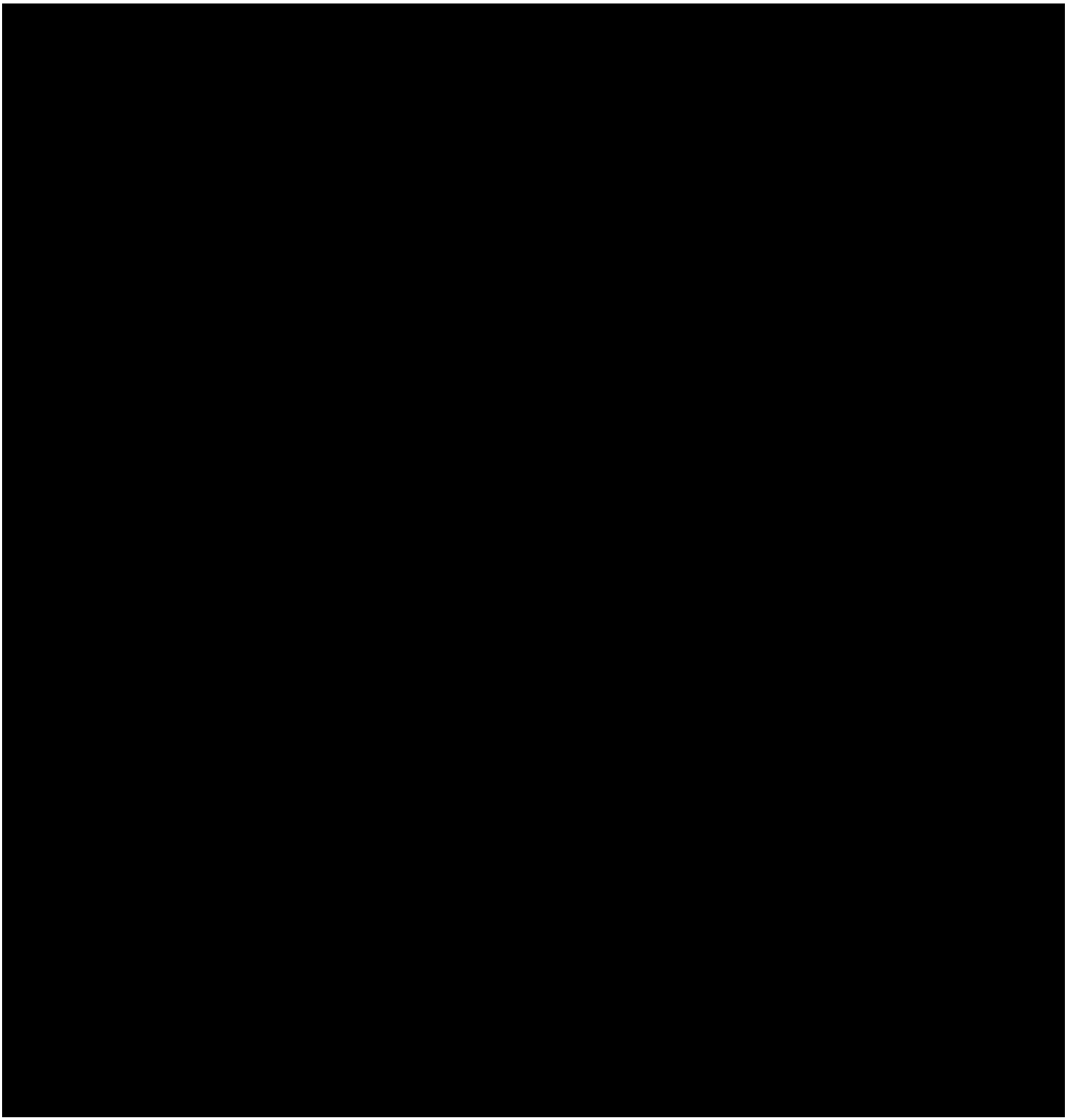

1.5.2 Faults

[redacted]

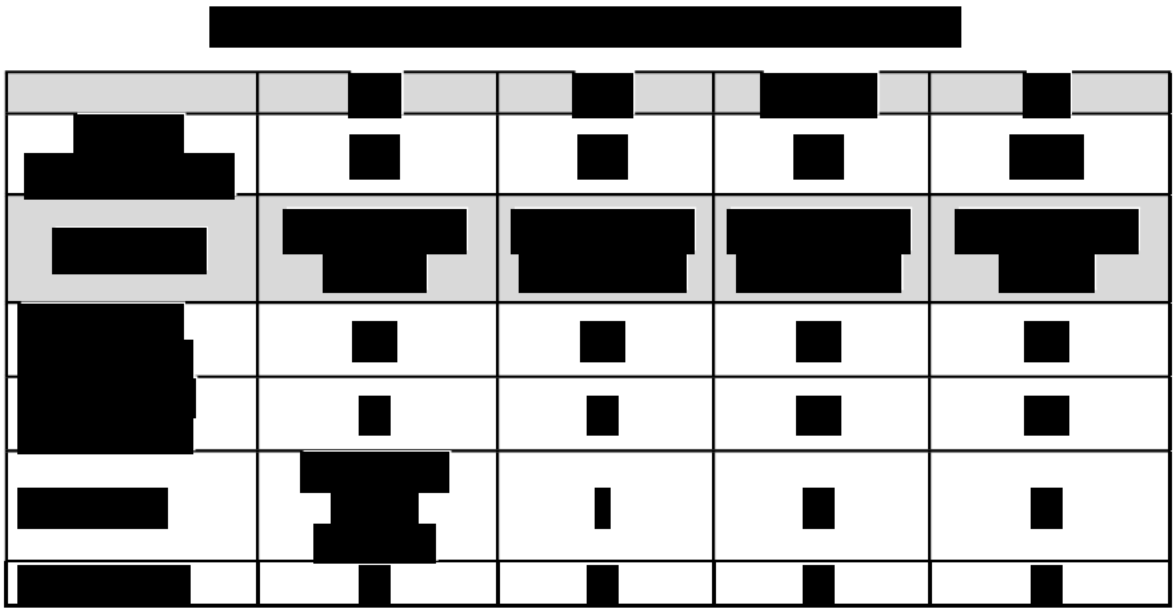

Shale gouge ratio (SGR) calculations to predict the fault seal quality were performed on all four faults. The SGR methodology is based on Yielding et al. (1997) (Figure 1-24), calculated by Equation 5, which utilizes the zone (lithology), thickness (h), clay fraction (Vshale, estimated from SP log (see *Section 1.4.3.1*)), and the fault displacement (fault throw). Calibrations were based on subsequent methods provided by Manzocchi et al. (1999) and Sperrevik et al. (2002). These calibrations conclude that permeability along the fault is ≤0.01 millidarcy (mD) with at least 50% clay fraction, or an SGR more than 0.5, or 50%. The SGR was evaluated using PE Limited's (Petex) MOVE software. For each fault, a well was chosen that (1) penetrates stratigraphy thought to be representative of that containing the most proximal extent of the pressure front and CO_2 plume; and (2) was judged representative of other wells along strike of the fault.

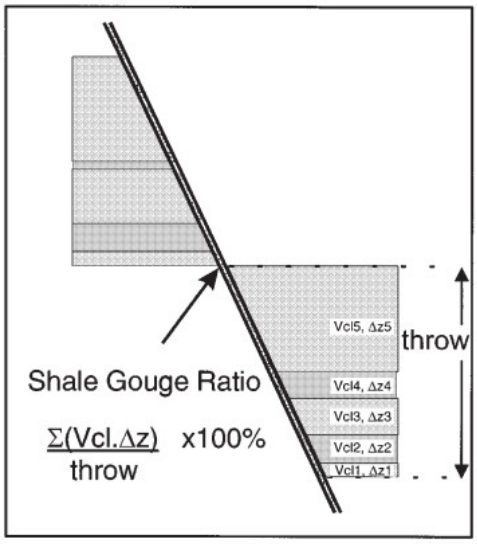

Figure 1-25 – Schematic of SGR Calculation from Yielding et al. (1997)

(Eq. 5)

$$SGR = \frac{\Sigma(h * VShal\ )}{Fault\ Throw}$$

[redacted]

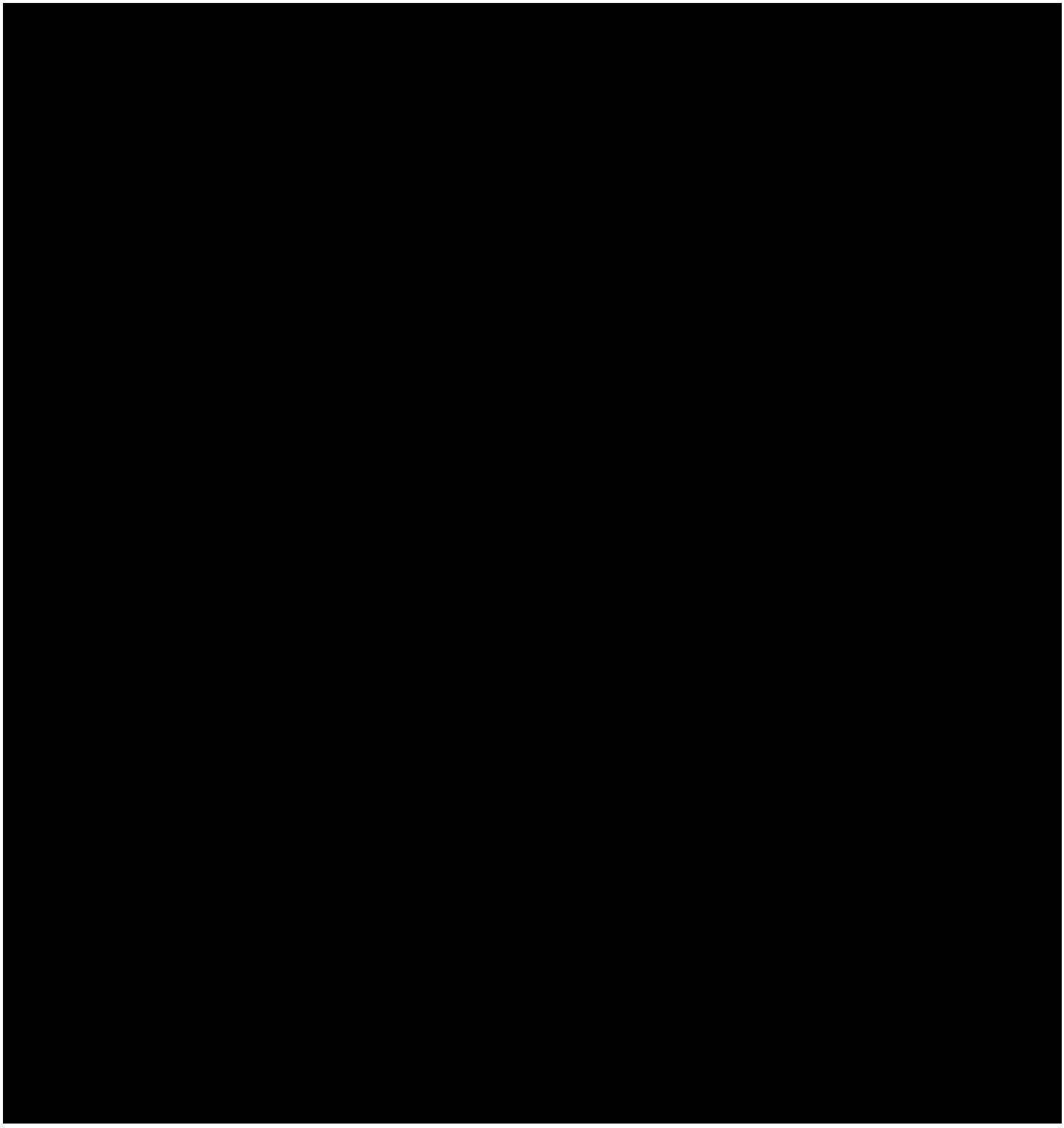

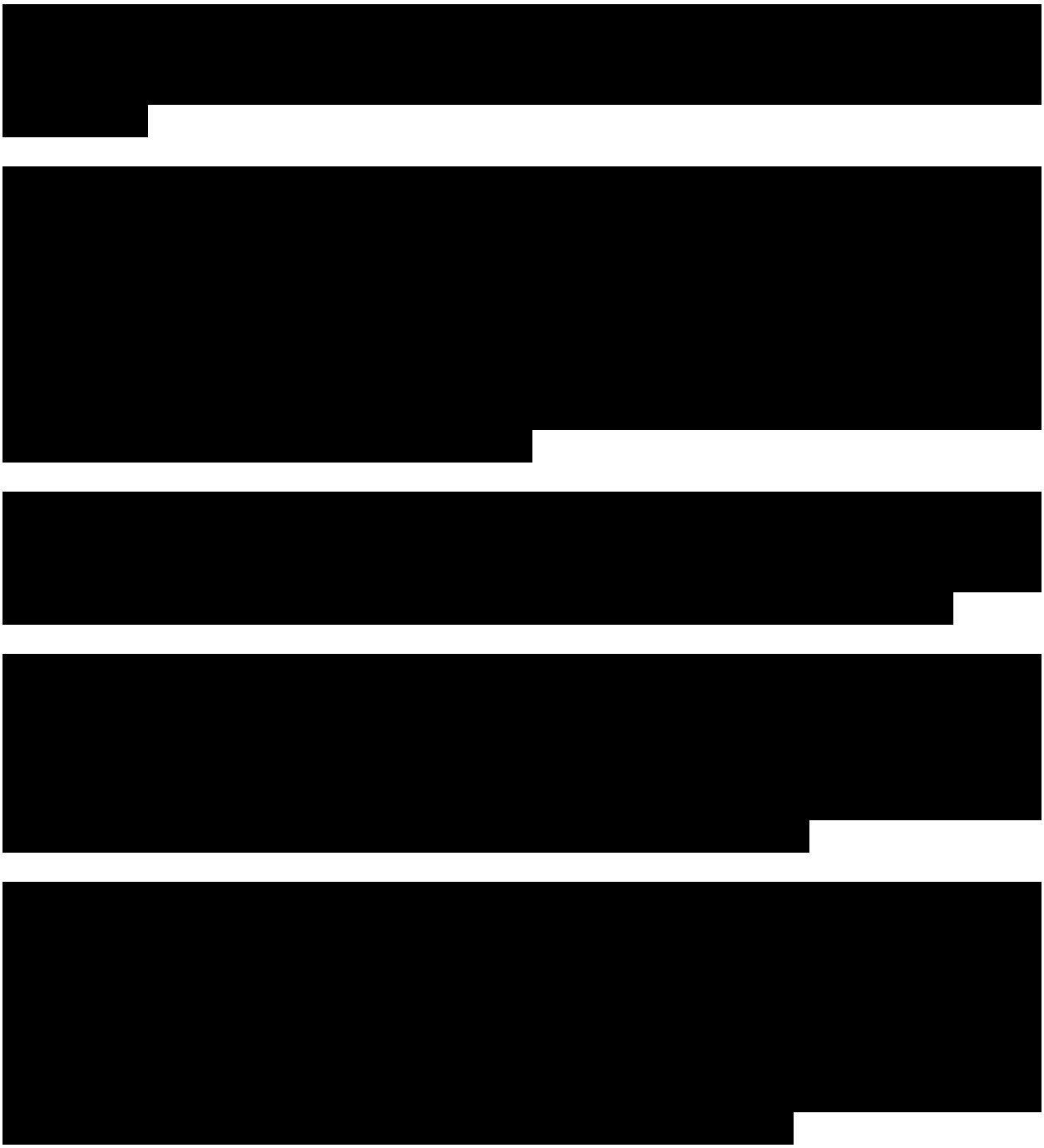

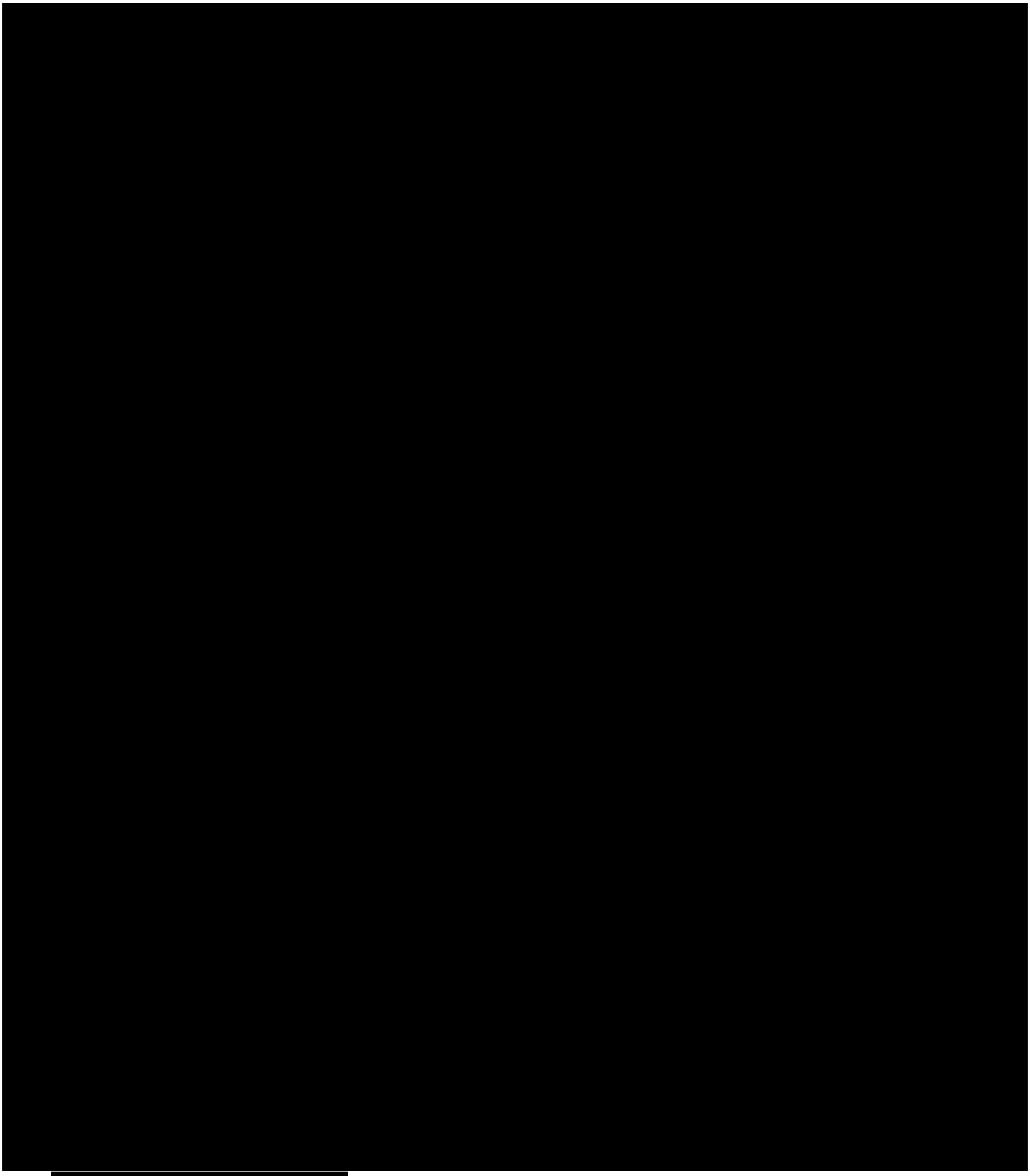

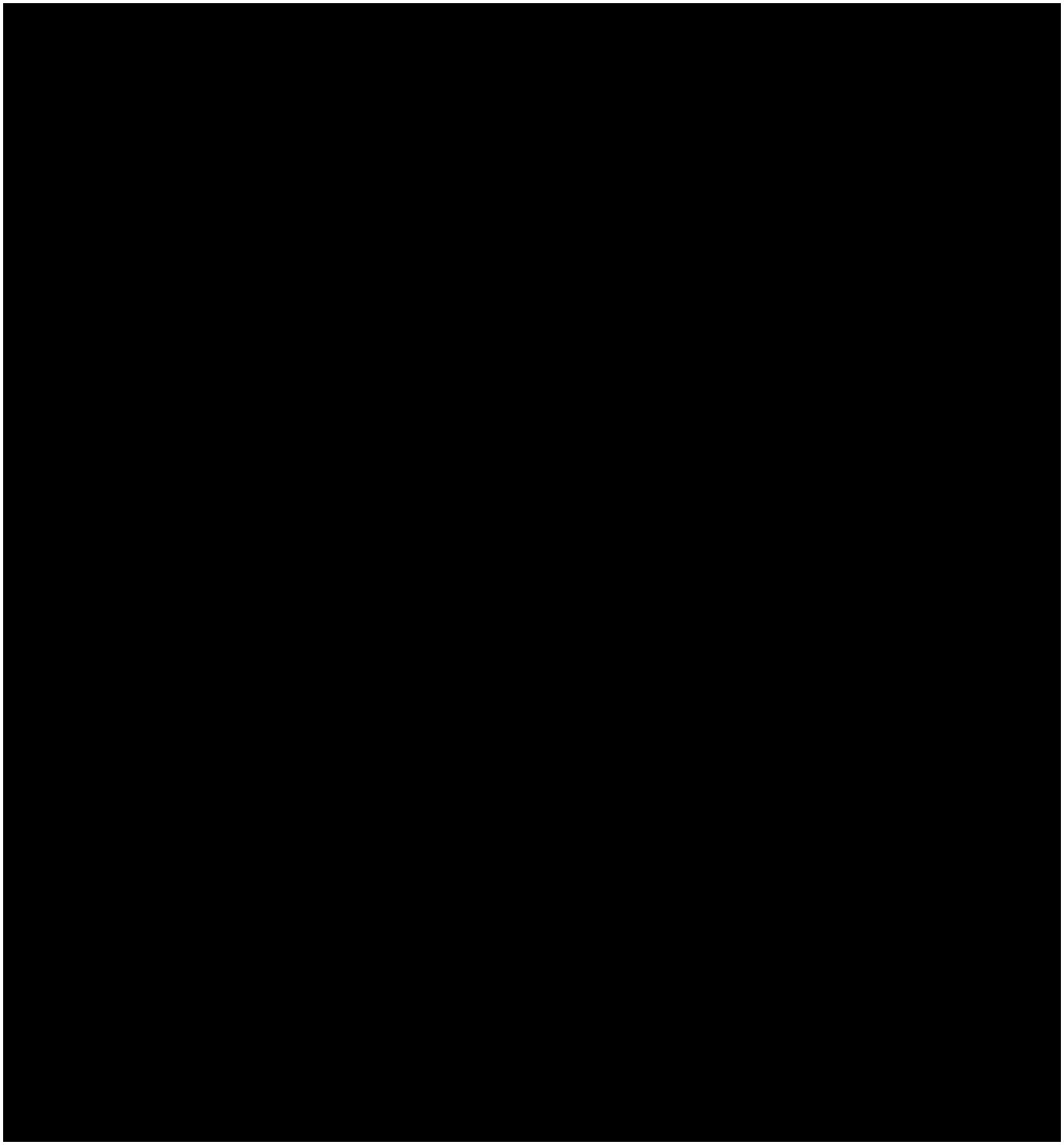

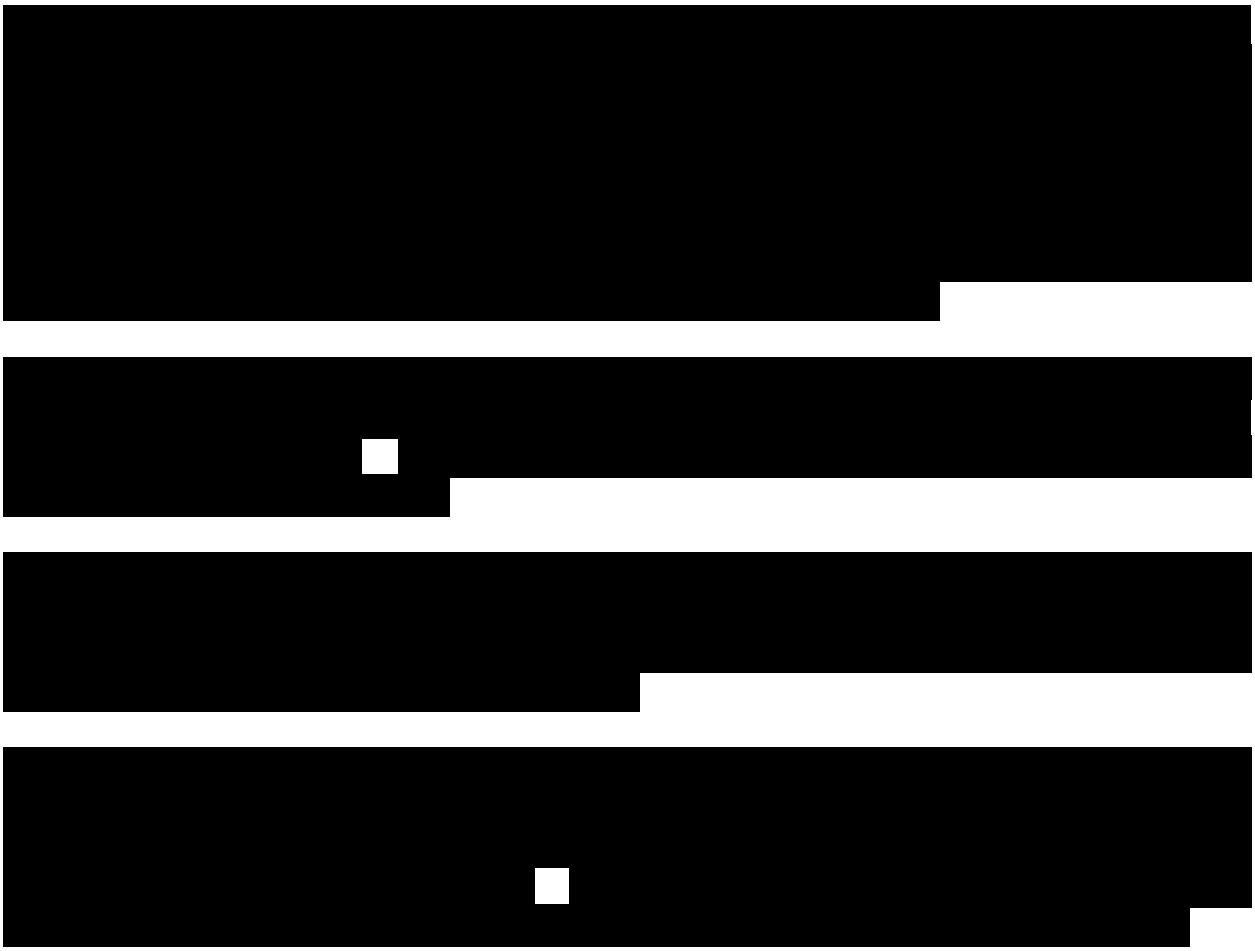

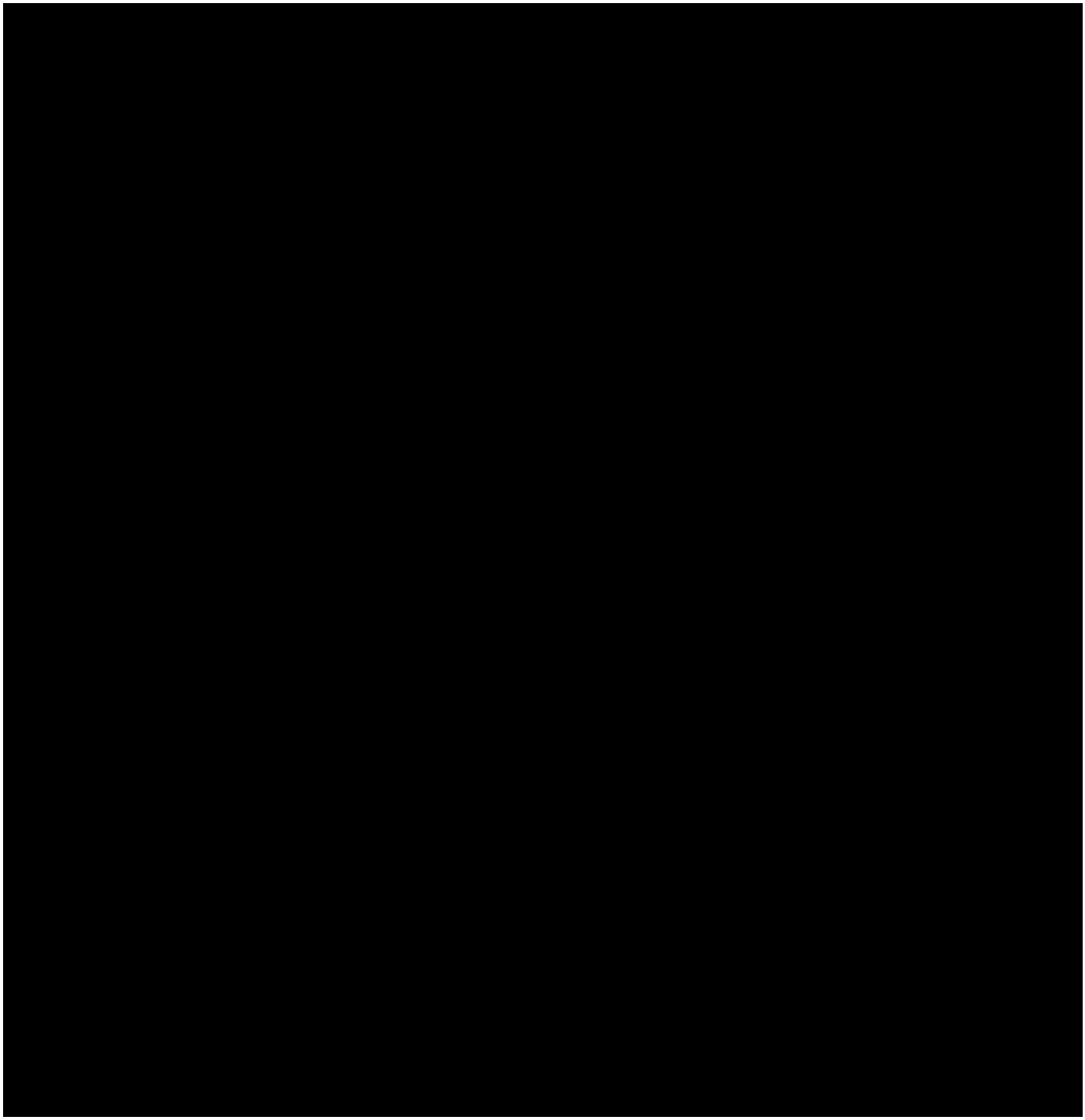

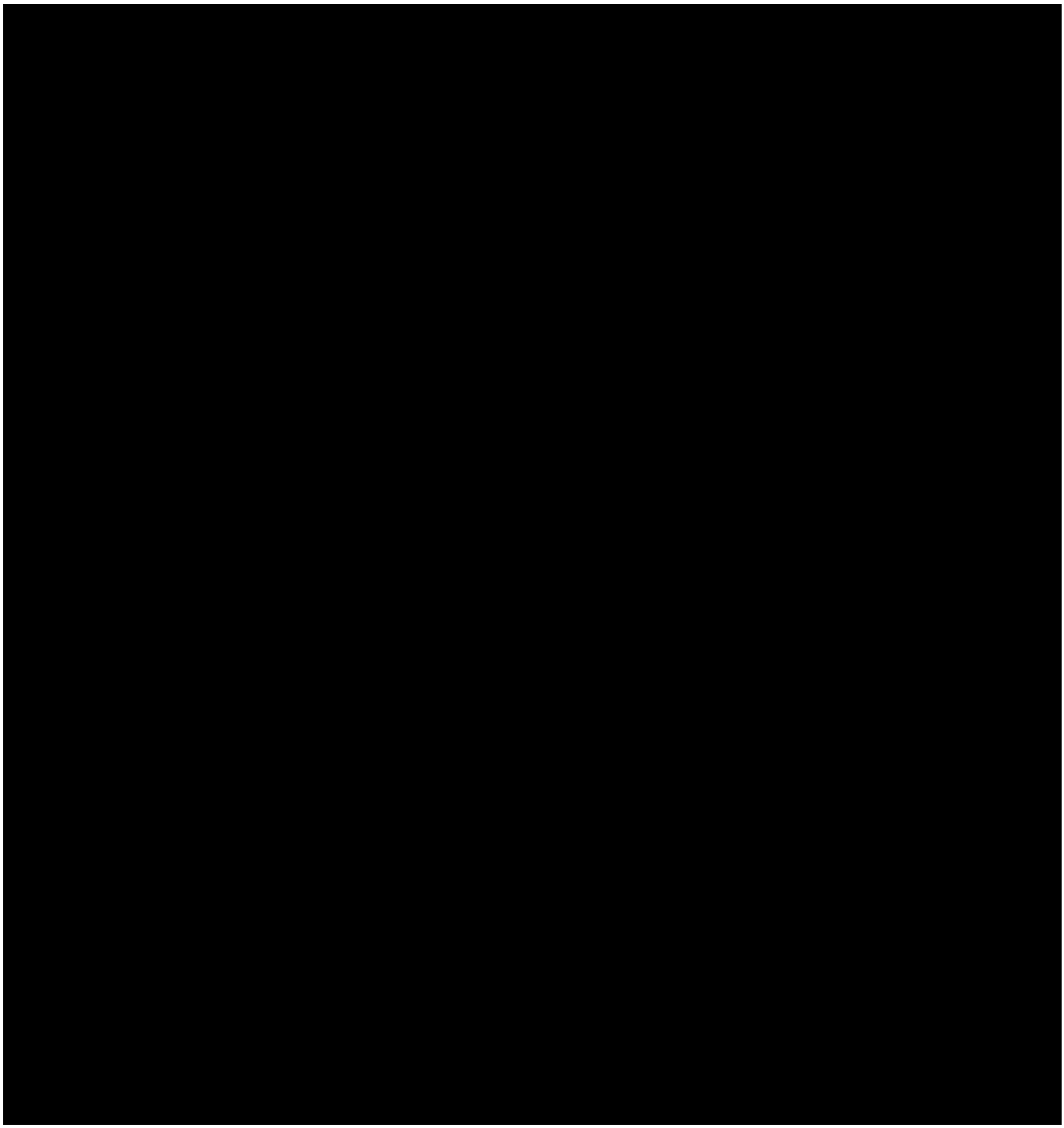

[redacted]

The local geologic setting is well-suited to the confident application of the SGR method to quantify the fault seal, because key geologic data requirements of the SGR method are locally met as follows:

1. During fault movement, the stratigraphic section was relatively unlithified. This both allows for the entrainment of low-permeability shale into the fault zone and precludes the preservation of open fractures along the fault zone. The geologically young Gulf Coast stratigraphy is relatively unlithified at present and would therefore have been unlithified during any past fault motion.

2. An appropriate calibration of SGR to fault seal and permeability is available. While a specific local calibration is not available, the SGR approach was developed and calibrated within globally analogous geologic settings. To address the lack of local calibration, ExxonMobil applied a conservative scaling of SGR to seal development. A higher SGR value corresponds to better fault seal development. For example, ExxonMobil limited seal development to SGR values greater than 0.5, while published calibration expects the onset of seal development at SGR greater than 0.2.

3. The well-based stratigraphy used in the SGR calculation is representative of the stratigraphy directly adjacent to the faults under consideration. Several well logs are available proximal/within the AOR, the majority being within [redacted] of the analyzed faults under consideration. In addition to leveraging the nearest well, the stratigraphy from a selection of other local wells was used to constrain allowable ranges of near-fault stratigraphic character. Importantly, the key identified sealing intervals [redacted] are stratigraphically continuous across the region and therefore are present in all of the local wells.

4. Fault architecture is described adequately to identify relevant features and accurately characterize fault throw. Available seismic data are sufficient to identify and characterize faults within and surrounding the AOR. [redacted] Additionally, smaller faults that are not identifiable on the available seismic surveys do not pose an additional seal uncertainty, because they host lesser amounts of stratigraphic offset (throw) by default.

1.6 Geomechanics

The information discussed in this section is from existing sources, such as publications and offset well data. Log data from existing wells around the Hummingbird Project region are used to estimate the local stress conditions, elastic moduli, and fracture gradients of the injection and confining zones.

1.6.1 Local Stress Conditions

The World Stress Map is a "global compilation of information on the crustal present-day stress field maintained since 2009 at the Helmholtz Centre Potsdam GFZ German Research Centre for Geosciences."[1] The associated website presents the compiled regional stress data, including that for the project region as shown in Figure 1-31. [redacted] stress regime is also inferred based on the World Stress Map.

[1] https://www.world-stress-map.org/

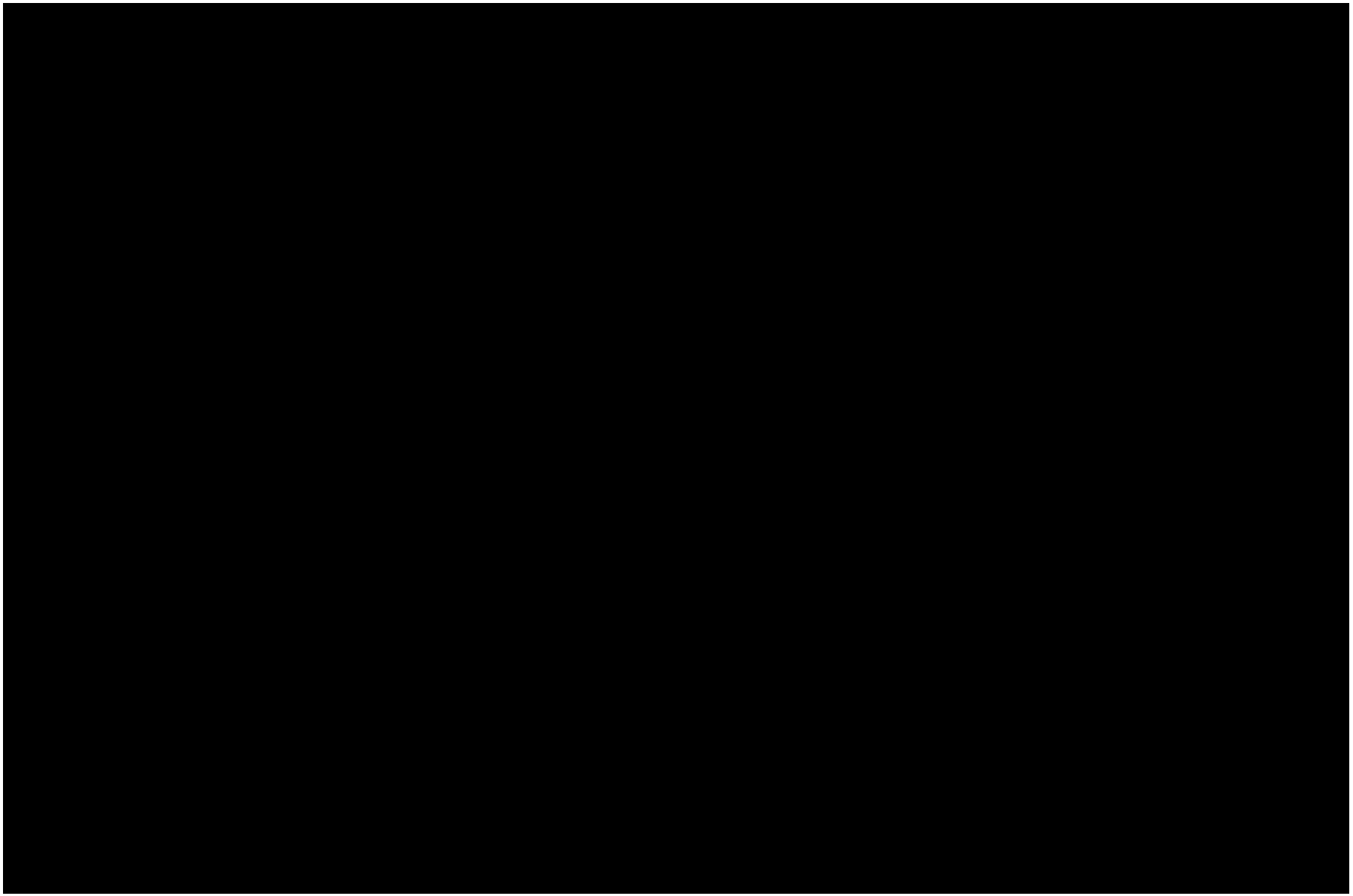

1.6.1.1 Vertical Stress

Vertical stress was characterized primarily using bulk density logs from offset wells—which Figure 1-32 shows near or in the project region—together with the density log [redacted] The figure indicates that formation bulk density in the area follows a similar trend, which can be approximated with an exponential fit. Integrating the density log derived with the exponential fit yields the overburden stress profile shown in Figure 1-32, [redacted]

[redacted]

1.6.1.2 Minimum Horizontal Stress

The minimum horizontal stress, utilized to estimate the fracture gradient, was calculated in two steps: (1) calculating a Poisson's ratio using available dipole sonic log data; and (2) using Eaton's equation to estimate the minimum horizontal stress and calibrate with available measurements. Dipole sonic log data have been collected in [redacted], where the compressional slowness (t_p) and shear slowness (t_s) log data are used in Equation 6 to calculate Poisson's ratio (ν):

(Eq. 6)

$$\nu = \frac{0.5\left(\frac{t_s}{t_p}\right)^2 - 1}{\left(\frac{t_s}{t_p}\right)^2 - 1}$$

Using the input parameters in Table 1-6 and Equation 6 at a depth of [redacted]

[redacted]

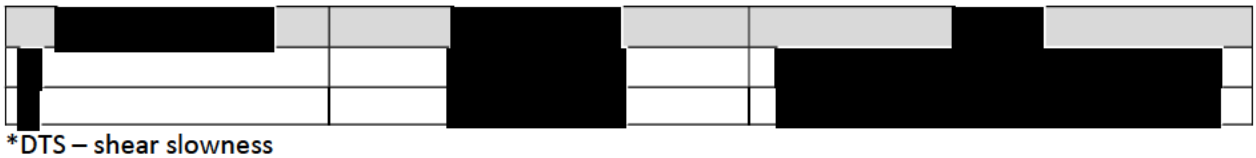

*DTS – shear slowness

Minimum horizontal stress is calculated using Eaton's equation, shown in Equation 7 where v is Poisson's ratio, S_V is the vertical stress, P_p is the pore pressure [redacted] while parameter C is a constant for calibration (tectonic stress) with available data.

(Eq. 7)

$$S_{hmin} = \frac{v}{1-v}\left(S_V - P_p\right) + P_p + C$$

Input parameters, shown in Table 1-7, were used in Equation 7 at a depth of [redacted]

[redacted]

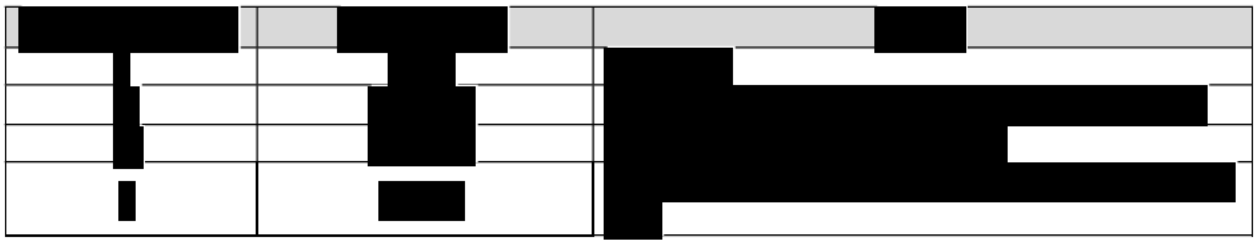

The result of these calculations shows the average best estimate, within the relevant formations, of the minimum horizontal stress for the selected well to be [redacted] with depth-dependent variations along the well, shown in Figure 1-33. Log data in this figure presents the sonic curves, the calculated Poisson's ratio curve, and the resulting minimum horizontal stress curve and its gradient.

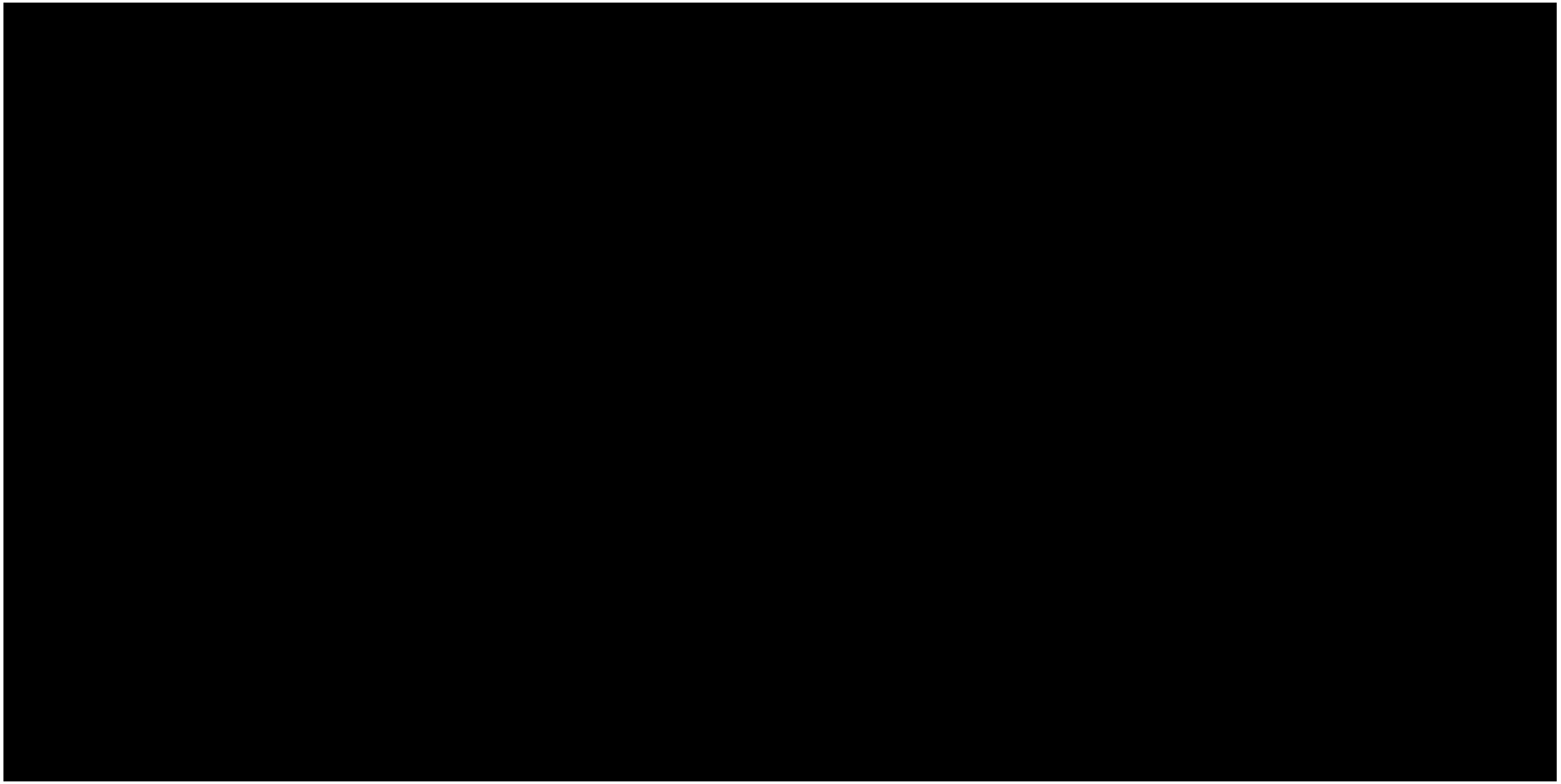

1.6.2 Elastic Moduli

Assuming that rock properties are isotropic, the dynamic Young's modulus (E_{dyn}) can be calculated using shear wave velocity and the Poisson's ratio (ν) as follows in Equation 8.

(Eq. 8)

$$E_{dyn} = 2\rho V_s^2(1+\nu)$$

where ρ is rock density and V_s is the shear wave velocity. As an example, the following input parameters (Table 1-8) were used in Equation 8 at a depth of [redacted]

[redacted]

*m/s – meters per second

A linear dynamic-to-static transform was used to convert dynamic Young's modulus into static Young's modulus (E_{sta}) as shown in Equation 9.

(Eq. 9)

$$E_{sta} = \mathrm{k}E_{dyn}$$

where *k* is a simple scaling factor and assumed to be [redacted] based on a lab test performed on representative core samples. An example of the workflow utilizing density and sonic logs to calculate Poisson's ratio and the Young's modulus is shown in Figure 1-34. The average Young's moduli in the proposed injection intervals are summarized in Table 1-9. Note that the density correlation defined in Figure 1-32 was used in the calculation, as no well in the area had both bulk density and dipole sonic log data over all of the injection intervals.

[redacted]

[redacted]		[redacted]		[redacted]	
[redacted]					

1.6.3 Fracture Gradient

1.6.3.1 Injection Zone

As discussed previously, Eaton's equation was used—with a pore pressure gradient of [redacted] to estimate the minimum horizontal stress in both sand and shale—and guided the estimate of the injection-zone fracture gradient. The minimum horizontal stress gradient over a sand interval is a conservative choice to represent the fracture gradient of the entire zone. The interpreted fracture gradients are shown in Table 1-10.

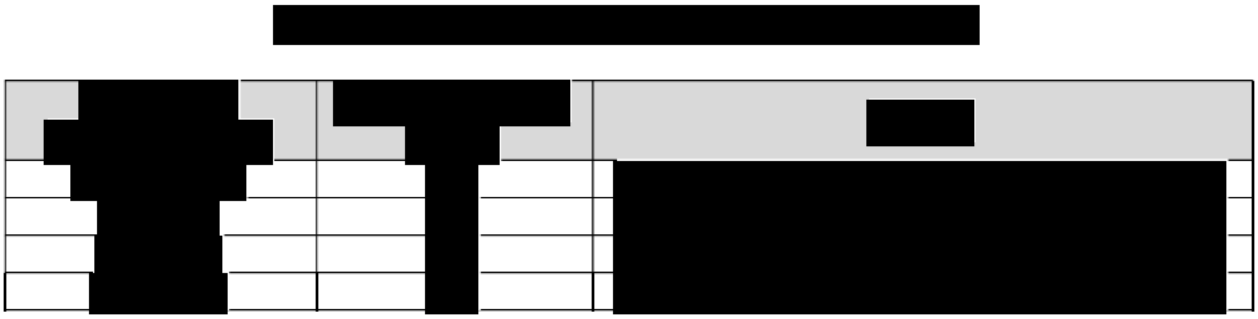

1.6.3.2 Confining Zone

Similarly, fracture gradients in the confining zone can also be evaluated. The calculated average values are shown in Table 1-11.

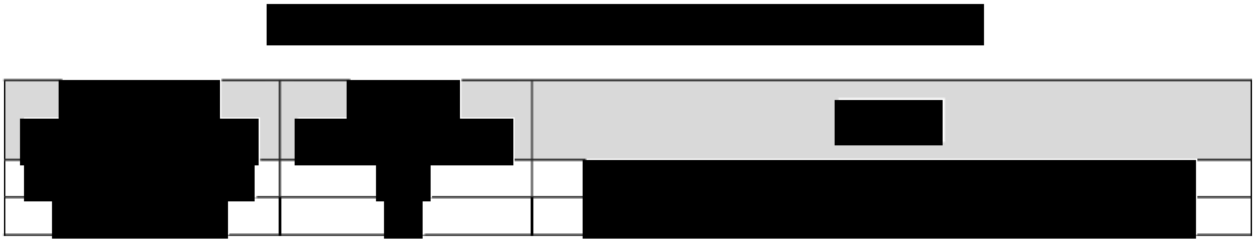

1.6.3.3 Maximum Injection Pressure Calculation

The maximum bottomhole injection pressure must not exceed 90% of the fracture pressure of the injection zone, to reduce the potential for existing fractures to propagate during normal operations. Using the estimated fracture gradient in Table 1-10, the maximum bottomhole injection pressures for the injection wells, at the top of each perforated interval, are shown in Table 1-12. Note that these estimates may be revised based on site data and updated well locations.

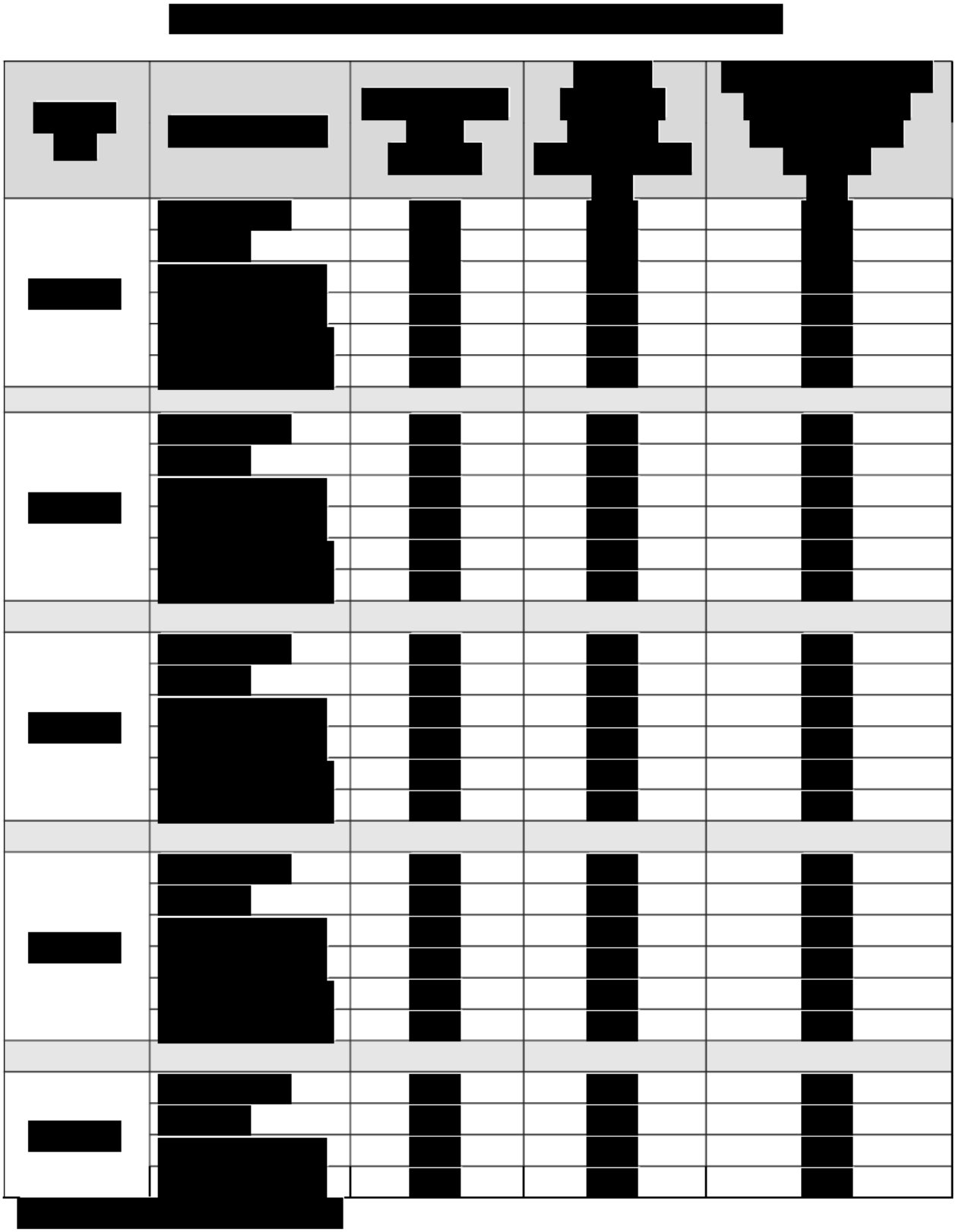

1.7 Baseline Geochemistry

1.7.1 Assessment of Injection Interval and Confining Zone Geochemical Reactions

Baseline geochemical information on the subsurface units in the AOR is provided based on preexisting data. Additionally, the evaluation of the injection intervals fluid geochemistry and mineralogy was conducted to assess the compatibility of the CO_2 stream with subsurface conditions. The objective of this assessment was to predict how storage and injectivity could be impacted by potential geochemical reactions, using regional brine and mineralogical data and kinetics-based, reaction-path geochemical models. The following discussion describes the potential for mineral dissolution and precipitation reactions to occur in the presence of a CO_2-saturated brine, and the impact of these chemical reactions on the total change in mineral volume and the pH of the brine phase.

Brine chemistry from available regional data in [redacted] (Figure 1-35) were modeled to be in equilibrium with the [redacted] In all models for each unit, the changes in mineral volume as a result of the chemical reactions that occur between the formation mineralogy and the CO_2-saturated brine were predicted to occur at a magnitude that is not expected to significantly impact the injectivity or storage capacity of the reservoir—or the integrity of the sealing unit.

1.7.2 Summary of Available Geochemical Brine Data

This preexisting fluid data was taken from the U.S. Geological Survey (USGS) National Produced Waters Geochemical Database (Blondes et al., 2023). This database contains information on the likely range of geochemical parameters and the nature of connate formation brines present in the proposed injection intervals. The major cation and anion composition of water samples used to derive the starting fluid chemistries incorporated into the models described below are provided in *Appendix B-3*. Select fluid sample compositions in *Appendix B-3* were outside of the likely range of fluids expected to be encountered in the AOR and were not included in the starting fluid chemistry used in the geochemical models. The starting fluid used in each unit- specific geochemical model will be updated following site-specific data collected in the stratigraphic test well, Hummingbird IZM No. 1

The fluid chemistry used for the [redacted] was used as the initial fluid chemistry and equilibrated with the representative mineralogy of the [redacted] (described below). The fluid chemistry for the [redacted] models. No data was available on the fluid chemistry in the [redacted]. There is uncertainty in the quality of the regional data due to the absence of duplicate and quality assurance samples. However, the average chemical composition of these existing fluid samples modeled to be in equilibrium with the expected formation mineralogy is believed to be representative of the subsurface fluids anticipated to be encountered in the AOR

formations of interest. Figure 1-35 shows the locations of wells from which preexisting data was taken for the geochemical models.

1.7.3 Modeling Approach for Potential Geochemical Reactions

The potential for brine-mineral-CO_2 interactions was modeled to assess the potential alteration of both the reservoir and sealing lithologies during and following CO_2 injection. The injection of CO_2 results in a decrease in pH as the CO_2 dissolves into the brine phase, forming carbonic acid, which dissociates rapidly to form bicarbonate and hydrogen ions. This decrease in pH shifts the brine-mineral system in disequilibrium, and subsequent mineral phase dissolution and precipitation reactions occur—increasing the pH and moving the system toward equilibrium with the altered brine chemistry. For example, anticipated fluid-mineral reactions include the

dissolution of feldspars to precipitate kaolinite, and the dissolution/precipitation of carbonates such as calcite (Gaus 2010; Shiraki and Dunn, 2000; Tang et al., 2021).

1.7.3.1 Reaction-Path Models

Simple kinetics-based, reaction-path models were developed using the Geochemist's Workbench (GWB) (Bethke et al., 2022) to trace mineral stability boundaries as chemical reactions progress, and to provide information on fluid evolution and mineral precipitation and dissolution. The models utilized here use a rate law expression and pH-dependent rate constants described in detail in Palandri and Kharaka (2004). Activation energies and neutral, acid, and base mechanism-rate constants used in the models are provided in *Appendix B-3*. The two major inputs for these models are the brine chemistry and the formation mineralogy. The composition of the injectate is assumed to be pure CO_2 for model simplicity. As the models presented are only concerned with the impact of CO_2 on the brine-mineral system, and the CO_2 is likely to represent the vast majority of the injectate, this assumption is not expected to impact the results significantly.

Model Input: Brine Chemistry

To obtain a representative fluid composition for the [redacted] the regional fluid data in *Appendix B-3* was averaged. Brine chemistry specific to the [redacted] The fluid is in equilibrium with quartz and feldspars; however, the analysis of the brine did not provide the concentrations of Al^{3+} or $SiO_{2\,(aq)}$. To estimate these fluid components, the SpecE8 module from GWB was used, setting $SiO_{2\,(aq)}$ and Al^{3+} concentrations to be controlled by the equilibrium solubility of quartz and albite, respectively, with the brine at the temperature and pressure of the formation. This model step also slightly alters the initial brine chemistry and total dissolved solids (TDS) to maintain charge balance.

Model Input: Formation Mineralogy

The representative primary mineralogy for [redacted] The averaged primary mineralogy used in the geochemical models and presented in *Appendix B-3* represents the major minerals that are likely to participate in chemical reactions with a CO_2-saturated brine in the subsurface at the injection site. Simplifications of the mineralogy are

necessary to maintain computational efficiency. The process of selecting minerals to represent the formation mineralogy in the geochemical models was developed through a step-by-step rationalization process, consistent with a typical geochemical modeling approach. Framework grains, such as quartz and feldspars, and carbonates were selected. Bulk clay was chosen to be represented by smectites, illite, and kaolinite. Pyrite/marcasite was included, when present, to assess concerns of the dissolution of sulfides.

Minerals that were not consistent throughout [redacted], or minerals not expected to significantly impact the modeling results (such as anatase), were not included in the models. For the [redacted], pyrite and marcasite were combined and represented as only pyrite. Albite was substituted for "plagioclase." [redacted]. As such, the method used by Xu et al. (2006) to estimate Na- and Ca-smectite, using the weight percent ratio of Na and Ca in the formation fluid, was used. [redacted] had no available mineralogical data and for the purpose of geochemical modeling the underlying [redacted] mineralogy was applied. Similarly, the [redacted] had no available mineralogical data and for the purpose of geochemical modeling the underlying [redacted] mineralogy was applied. Geochemical modeling will be updated following site-specific data collected in the stratigraphic test well, Hummingbird IZM No. 1.

Simulating Initial Brine-Mineral Equilibrium and CO_2 Reactions

Before adding CO_2 to the brine-mineral system, the averaged brine chemistry was equilibrated with the formation mineralogy over a 1,000-year model simulation period in the React Module of GWB. The equilibrated fluid compositions from React used in the kinetics-based, reaction-path models are provided in *Appendix B-3* along with TDS, estimated formation temperature, and pH. The React Module was also used to simulate CO_2 injection into the initial brine-mineral equilibrated system. The amount of CO_2 gas dissolved into the brine solution was limited to its solubility at subsurface conditions (pressure, temperature, and brine salinity) for each modeled interval. The CO_2 solubility was calculated using Duan and Sun (2003). The CO_2 was added to the model until the solubility limit was reached, at which point the CO_2 gas fugacity was fixed to simulate a system of a CO_2-saturated brine that is in contact with a separate CO_2 fluid phase. This is expected to occur quickly and, as such, this variable CO_2 gas-fugacity step was modeled to occur within 0.05 years.

The chemical reactions that occur during the fixed CO_2 gas-fugacity model step were simulated for a 100-year period. During this time, secondary minerals may become saturated in the brine phase and precipitate. The secondary minerals used in the models were chosen based on the saturation index of various minerals at the end of a preliminary fixed-fugacity model for each formation. The secondary minerals with a saturation index greater than unity were given proper kinetics, and the fixed-fugacity model was rerun, allowing these phases to precipitate. *Appendix B-3* lists the observed secondary minerals for each model. The thermo.com.V8.R6+.tdat database (Wolery, 1992), modified to include thermodynamic data on ankerite, was used in all models. This database was extrapolated to the formation pressures using the R script "logKcalc"

written by Jeffery Dick (Dick, 2024). *Appendix B-3* also lists the relevant chemical formulae of the modeled minerals.

1.7.4 Summary of Geochemical Modeling Results and Findings

The geochemical models were used to simulate the potential for significant mineral precipitation and dissolution to occur in the injection and confining intervals. *Appendix B-3* presents the geochemical modeling results for the [redacted]. The results are plotted as change vs. time for the following relationships:

- Mineral weight percent change vs. elapsed time (A). A positive slope indicates that the mineral is precipitating, and a negative slope indicates that the mineral is dissolving.
- The pH of the brine vs. time (B)
- The total mineral volume change vs. time (C). An increase in total mineral volume corresponds to a decrease in porosity and vice versa.

The following findings are apparent from the review of the geochemical models and the trends in mineral phase dissolution and precipitation:

- All geochemical models predict that, during the interaction of CO_2-saturated brine and formation mineralogy, both precipitation and dissolution of minerals occur at a magnitude that does not alter the volume of the minerals significantly enough to result in a material change to the CO_2 sequestration capacity of the injection interval or the integrity of intraformational sealing units. In the injection interval cases, the volume percent change was predicted to be less than 0.04 volume percent. In the intraformational seal cases, the volume percent change was predicted to be less than 0.7 volume percent.

- The presence of calcite and dolomite in the primary mineralogy is predicted to buffer the pH of the system to a steady state within approximately 25 years for the injection intervals and approximately two years for the intraformational seals. This pH value will remain relatively constant until the brine is no longer in contact with the separate CO_2 phase. Though not modeled here, it is expected that the CO_2-saturated brine-mineral system without a separate CO_2-rich fluid phase would tend toward higher pH values (see, for example, Zerai et al., 2006).

1.7.5 Potential Uncertainty in Geochemical Reaction Path Model

A review of the input data and geochemical model performance identified the potential for uncertainty to influence the model results. As outlined below, steps were taken to reduce the potential for the uncertainty in site characterization and the modeling approach to impact the overall findings of the geochemical model.

There is uncertainty involved in using laboratory-derived kinetics to model natural systems. Laboratory-derived rate constants tend to be several orders of magnitude larger than what is

observed in nature (Brantley, 1992). This is due to several factors, such as limited contact of fluid with minerals, and surface area impacted by natural processes. Other potential sources of error introduced by the use of kinetics include reactions occurring at laboratory conditions that are not predominate in nature, and the impact of bacteria on reaction rates (Bethke, 2022). However, as no significant impact of mineral precipitation/dissolution was predicted by the models using these laboratory-derived kinetics, it is not expected that the natural system would be significantly impacted either, as the natural rates are likely to be slower (Brantley, 1992).

Modeling brines with a high salinity is difficult for several programs, including GWB (Bethke, 2022; Allen et al., 2005)—which has a default limitation on the ionic strength of the brine used as the basis set of 3 molal. This is sufficient for both formation fluids modeled here. Further, to account for the salting-out effect of CO_2, the ion size parameter of $CO_{2\,(aq)}$ was adjusted to -0.5 (Allen et al., 2005; Zerai et al., 2006).

The analytical results for brine samples did not include dissolved SiO_2, K^+, and Al^{3+}, typically derived from the dissolution of quartz and feldspars. Estimated equilibrium concentrations were derived using the SpecE8 module from GWB. This approach has been shown to provide reasonable initial concentrations for reaction-path modeling. The resulting precipitation and dissolution of mineral phases were reviewed to reduce the potential for unrealistic precipitation simulated by the model. None were found.

1.7.6 Summary of Predicted Geochemical Reactions

A series of geochemical scenarios were modeled to provide predictions on the compatibility of the injection intervals [redacted] and sealing intervals [redacted]) expected to be encountered in the AOR, with the injection of CO_2 and the subsequent CO_2-saturated brine. These models used regional fluid chemistry and XRD mineralogical data representative of the units of interest. All models demonstrated that, during the interaction of the CO_2-saturated brine and the units of interest, both precipitation and dissolution of minerals are predicted to occur at a magnitude that does not alter the volume of the minerals significantly.

1.8 Hydrology

The following hydrologic review of Allen Parish was conducted for the Hummingbird Project to properly characterize and protect potential water resources in the state of Louisiana. The study reviewed publicly available material published by the LDENR via their Strategic Online Natural Resources Information System (SONRIS), the USGS, and literature from peer-reviewed journals. The LDENR and SONRIS online databases supplied helpful documents regarding water well and groundwater information. Studies released by the USGS also contributed to the hydrologic evaluation and were utilized to source figures included in this section.

1.8.1 Water Resources of Allen Parish

Allen Parish is located in southwestern Louisiana and covers an area of approximately 766 square miles (Figure 1-36). The average water withdrawal from Allen Parish in 2005 was approximately

29.2 million gallons per day (Mgal/d), sourced from both groundwater (26.75 Mgal/d) and surface water resources (2.45 Mgal/d). The Chicot, Evangeline, and Jasper aquifer systems represent the primary sources of fresh groundwater potential in the parish—for rice irrigation, public supply, aquaculture, rural domestic, general irrigation, industrial, and livestock uses. The Chicot and Evangeline aquifer systems contain freshwater throughout Allen Parish, whereas the deeper Jasper aquifer system tends to only contain freshwater in the northwestern portion of the parish. Surface water contributions within the parish occur from the Calcasieu River (2.10 Mgal/d), Bayou Blue (0.33 Mgal/d), and other miscellaneous streams (0.02 Mgal/d) (Prakken, Griffith, and Fendick, 2012).

The stratigraphic column displayed in Figure 1-37 clarifies local and regional stratigraphic nomenclatures of freshwater-bearing aquifers in southwestern Louisiana. The schematic cross sections provided in Figures 1-38 and 1-39 clarify the structural and stratigraphic relationships of these formations through southwestern Louisiana and Allen Parish.

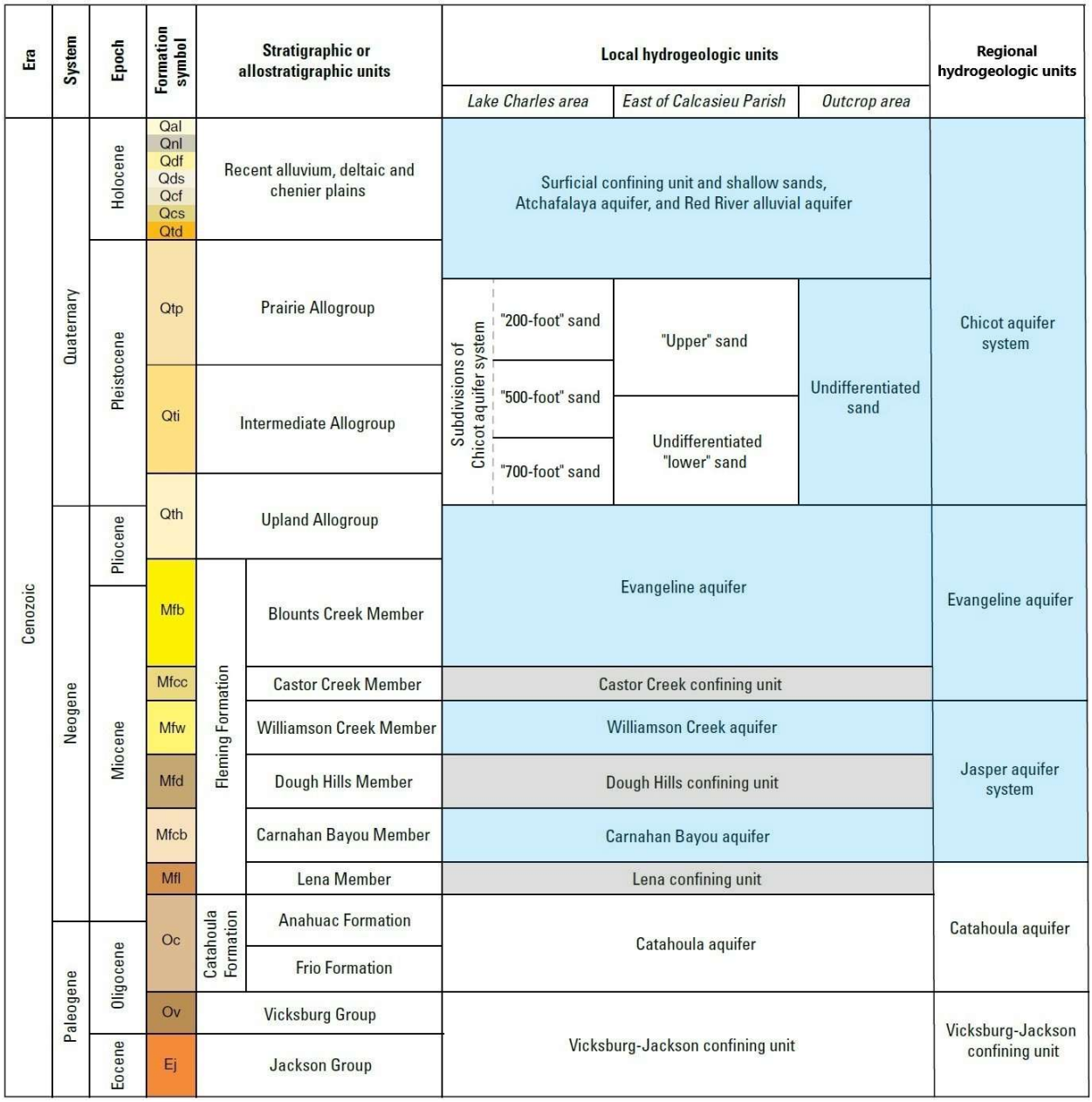

Figure 1-37 – Stratigraphic column of southwestern Louisiana with regional and local hydrogeologic units (modified from Lindaman, 2023). Formations with freshwater potential in Allen Parish are signified with blue shading.

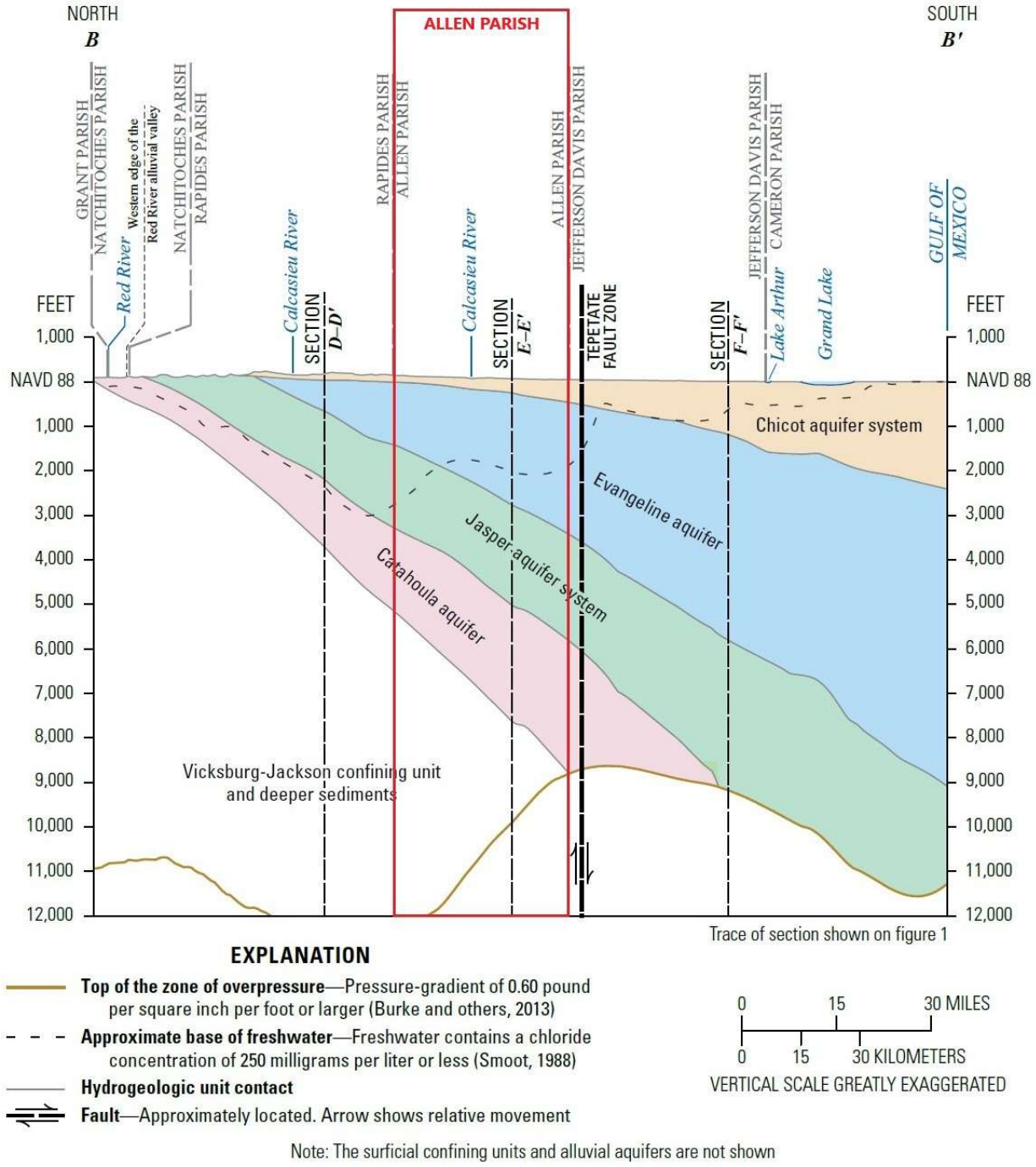

Figure 1-38 – Schematic north-to-south hydrogeologic section (B-B') through southwestern Louisiana (modified from Lindaman, 2023), with the red line clarifying the section in Figure 1-36.

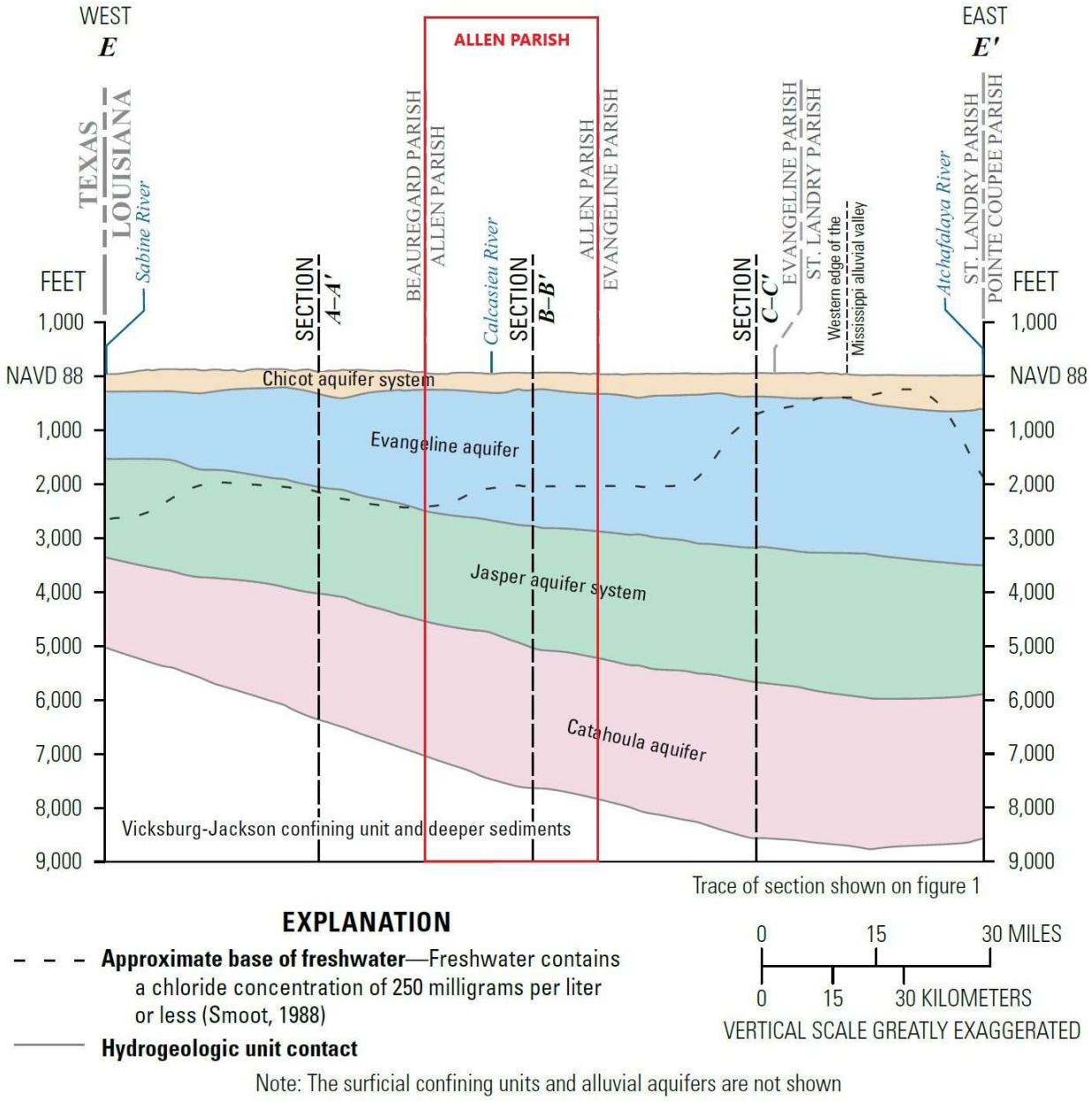

Figure 1-39 – Schematic west-to-east hydrogeologic section (E-E') through southwestern Louisiana (modified from Lindaman, 2023), with the red line clarifying the section in Figure 1-36.

1.8.2 Chicot Aquifer System

The Chicot aquifer system consists of a series of shallow Pleistocene deposits that span over 9,000 square miles across southwestern Louisiana into portions of the Texas coastal lowlands. Aquifers are present within silt, sand, and gravel deposits interbedded with clay and sandy clay that dip and thicken toward the Gulf of Mexico (Figures 1-40 and 1-41). Moving south, deposits tend to grade from coarse sand and gravel to finer sediments that are increasingly subdivided by

clay intervals (Lovelace et al., 2002). In Allen Parish, the Chicot aquifer system is comprised of an undifferentiated sand interval overlain by a surficial confining unit of sand, silt, and clay (Prakken et al., 2012).

Shallow Sand Deposits

Shallow sand deposits occur as discontinuous sand streaks, lenses, and layers within the surficial clay confining unit (Figure 1-42). Gross thickness of the surficial confining unit typically ranges between 40–80 feet in the parish but can thin to less than 40 feet in some areas. According to the USGS Water Resources of Allen Parish report (2012), there were 75 active water wells screened in the shallow sand in 2010. Reported water well depths ranged from 13–100 feet below land surface and total water withdrawals averaged 0.09 Mgal/d (Prakken et al., 2012).

Undifferentiated Sand Interval

The undifferentiated sand interval underlies the surficial confining unit and generally consists of discrete interbeds of clay, silt, sand, and gravel. Sand deposits are typically massive and tend to fine upward through the section, from coarse sand and gravel to fine sand; these deposits can reach up to several hundred feet thick. The base of the undifferentiated sand in Allen Parish ranges from ground level in the north to approximately 400–500 feet below the North American Vertical Datum of 1988 (NAVD 88) in southern portions of the parish (Figure 1-40). The undifferentiated sand is present throughout the parish and supplies the majority of freshwater from the Chicot aquifer. According to the USGS Water Resources of Allen Parish, there were 443 active water wells screened in the undifferentiated sand in 2010. Reported water well depths ranged from 16–450 feet below land surface with a median depth of 130 feet. Reported yields from the undifferentiated sand varied from 10–7,000 gallons per minute (gal/min) with a total average water withdrawal of 23.0 Mgal/d (Prakken et al., 2012).

1.8.3 Characteristics of the Chicot Aquifer System

Recharge and Discharge

The primary source of recharge to the Chicot aquifer system in Allen Parish is from direct infiltration of precipitation where the aquifer outcrops in Allen, Beauregard, Rapides, and Veron Parishes. Secondary recharge to the aquifer is supplied from vertical leakage through surrounding clays and natural flow from rivers and streams. Discharge from aquifers in Allen Parish generally occurs from water well withdrawals, surface flow into rivers, and communication with underlying aquifers (Prakken et al., 2012).

Potentiometric Surface and Groundwater Flow Direction

Groundwater tends to move within aquifers from areas of higher hydraulic head to areas of lower hydraulic head and the flow direction is generally perpendicular to potentiometric surface contours. A potentiometric surface map of the Chicot aquifer system published by the USGS is

provided in Figure 1-42. The map demonstrates that groundwater should flow from northwest to southeast within the project area, in agreement with interpretations published by Prakken et al. (2012).

Water Quality

Table 1-13 displays a statistical summary of water-quality characteristics from the 2012 USGS Water Resources of Allen Parish. The study sourced data from 81 wells screened in the undifferentiated sand interval of the Chicot aquifer system in Allen Parish between 1940 and 2008. Water from the undifferentiated sand is generally soft, with a calcium carbonate content below 60 milligrams per liter (mg/L). Median concentrations of manganese are 55 micrograms per liter (µg/L) and generally exceed the EPA's secondary maximum contaminant levels (SMCLs) of 50 µg/L for drinking water. Median iron concentrations are 200 µg/L but exceed the SMCL of 300 µg/L in some portions of Allen Parish. The median pH is 6.2, slightly more acidic than the SMCL suggested range of 6.5–8.5 (Prakken et al., 2012).

Table 1-13 – Water-quality characteristics of freshwater from the Chicot aquifer system (undifferentiated sand) and Evangeline aquifer system in Allen Parish (Prakken et al., 2012).

	Temperature (°C)	Color, (PCU)	Specific conductance, field (µS/cm at 25°C)	pH, field (SU)	Hardness (as $CaCO_3$)	Chloride, filtered (as Cl)	Iron, filtered (µg/L as Fe)	Manganese, filtered (µg/L as Mn)	Dissolved solids, filtered
Chicot aquifer system (undifferentiated sand), 1940–2008 (81 wells)									
Median	20.7	5	151	6.2	30	18	200	55	120
10th percentile	20.0	0	62	5.3	6	5.5	<10	<1	46
90th percentile	21.5	28	271	7.9	73	32	6,700	540	206
Number of samples	51	13	55	44	59	80	31	28	40
Percentage of samples that do not exceed SMCLs	NA	77	NA	41	NA	100	55	50	100
Evangeline aquifer, 1946–95 (44 wells)									
Median	23.5	10	321	8.2	5	8.0	230	20	230
10th percentile	21.5	5	255	7.2	2	4.8	50	0	193
90th percentile	25.0	140	764	8.6	26	25	870	76	494
Number of samples	33	41	42	43	43	44	41	33	40
Percentage of samples that do not exceed SMCLs	NA	59	NA	84	NA	100	61	85	90
SMCLs									
	NA	15	NA	6.5–8.5	NA	250	300	50	500

[Values are in milligrams per liter, except as noted. °C, degrees Celsius; PCU, platinum cobalt units; µS/cm, microsiemens per centimeter; SU, standard units; $CaCO_3$, calcium carbonate; µg/L, micrograms per liter; <, less than; NA, not applicable; SMCL, Secondary Maximum Contaminant Level established by the U.S. Environmental Protection Agency (2011)]

1.8.4 Evangeline Aquifer System

The Evangeline aquifer system underlies the Chicot aquifer system and is composed primarily of fine- to medium-grained sand with interbeds of silt, clay, and localized coarse sand lenses. Permeable sand deposits of the aquifer system tend to be separated by extensive confining clay intervals that can restrict communication (Prakken et al., 2012). Sands encased within upper portions of the system are saturated with freshwater, while lower sand beds tend to be saturated with brackish to saline water (Angel and Whiteman, 1985). This is illustrated by the base of freshwater contact displayed on the regional cross section provided in Figure 1-38.

The base of the Evangeline aquifer system ranges from approximately 1,500 feet below NAVD 88 in northern Allen Parish to approximately 3,500 feet below NAVD 88 in southern portions of the parish, as illustrated on the structure map in Figure 1-43. Gross thickness of the aquifer system ranges from approximately 1,500–3,000 feet in the parish, thickening toward the south-southeast (Figure 1-44) (Lindaman, 2023). Sands bearing freshwater have an aggregate thickness of approximately 1,000 feet in central-western Allen Parish and thin to approximately 200 feet along the southern parish line. The aquifer is present throughout the parish and provides approximately 13.7% of groundwater to the parish, with the remainder supplied by the Chicot aquifer system. According to the USGS Water Resources of Allen Parish, there were 34 active

water wells screened in the Evangline aquifer system in 2010. Reported water well depths ranged from 390–1,720 feet below land surface with a median depth of 749 feet. Reported yields from the undifferentiated sand varied from 9–1,000 gal/min with a total average water withdrawal of 3.68 Mgal/d (Prakken et al., 2012).

1.8.5 Characteristics of the Evangeline Aquifer System

Recharge and Discharge

Recharge off of aquifers in Allen Parish generally occurs from precipitation, hydraulic communication with overlying aquifers, and season inflow from rivers. Discharge from aquifers in Allen Parish generally occurs from water well withdrawals, surface flow into rivers, and communication with underlying aquifers (Prakken et al., 2012).

Base of Freshwater

Figure 1-45 portrays a structure map of the base of fresh groundwater across Allen Parish with a red star signifying the approximate location of the Hummingbird Project area. The base of fresh groundwater contact varies within Allen Parish and acts independent of aquifer systems, but generally ranges between 1,500–3,500 feet below the National Geodetic Vertical Datum of 1929 (NGVD 29) (Prakken et al., 2012). The base of freshwater occurs most often within the Evangline aquifer system—except in northern Allen Parish, where present within the Jasper aquifer system. This is illustrated by the base of freshwater contact displayed on the regional cross section provided in Figure 1-38. Nine wells identified in SONRIS contain USDW-base depth determinations proximal to the project area [redacted]. The reported base of USDW depths range between [redacted] and are consistent with the structure map provided in Figure 1-43 and associated base of freshwater depths reported by Prakken et al., (2012).

Potentiometric Surface and Groundwater Flow Direction

Groundwater tends to move within aquifers from areas of higher hydraulic head to areas of lower hydraulic head with a general flow direction perpendicular to potentiometric surface contours. A potentiometric surface map of the Evangeline equivalent aquifer system published by the USGS is provided in Figure 1-46. The map demonstrates groundwater has a general flow direction to the south-southeast within the project area, in agreement with interpretations published by Prakken et al., (2012).

Water Quality

A statistical summary of water-quality characteristics from the 2012 USGS report discussing Water Resources of Allen Parish was provided in Table 1-13. The study sourced data from 44 wells screened in the Evangeline aquifer system in Allen Parish between 1946 and 1995. Water

sampled from freshwater portions of the aquifer is generally soft and within SMCL tolerances for drinking water. Concentrations of iron and manganese slightly exceed suggested SMCLs within select portions of Allen Parish (Prakken et al., 2012).

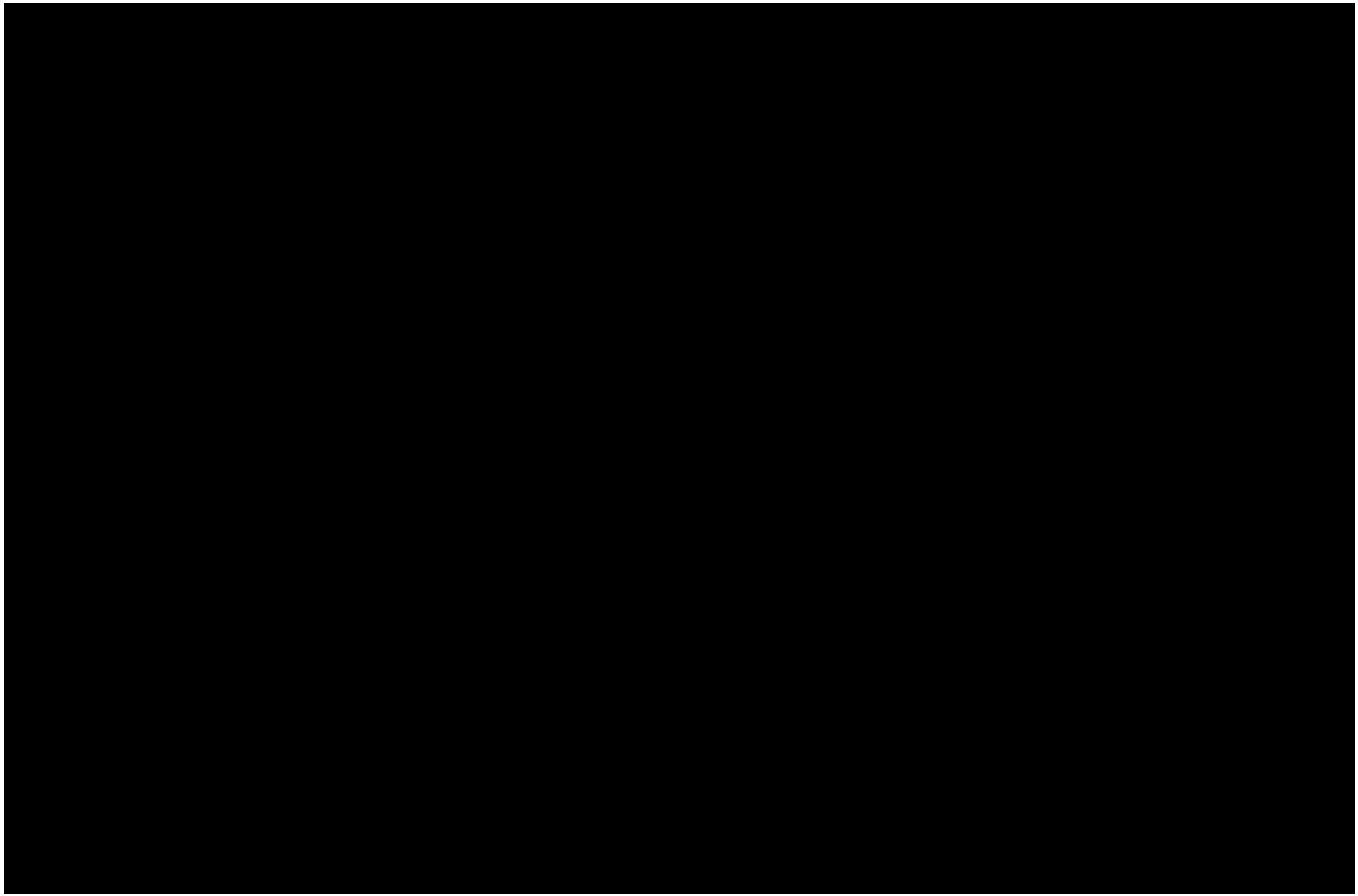

1.8.6 Jasper Aquifer System

The Jasper aquifer system is present throughout Allen Parish but only contains freshwater in northwestern portions of the parish. Downdip, in the vicinity of the AOR, the Jasper aquifer system is equivalent to the [redacted]. The base of freshwater becomes progressively shallower moving southeast in Allen Parish, while regional dip continues to deepen and aggregate thickness of freshwater sands to thin. As a result, there is a limited window of freshwater potential in the aquifer system. According to the USGS Water Resources of Allen Parish, there were no active water wells screened in the Jasper in 2010. Water sampled from test holes drilled in freshwater-bearing areas of the Williamson Creek aquifer in Allen Parish suggest that the water is soft but exhibits an alkaline pH over 8.0 and iron concentrations that exceed the SMCL of 300 µg/L (Prakken et al., 2012).

1.8.7 Base of USDW Determination

For the Hummingbird Project, the base of the lowest USDW was determined from public data, review of offset wells and literature review. The lowest USDW base was determined using a resistivity log-based method outlined by the LDENR. This method uses the deep induction curve of the electric log along with depth and resistivity cutoffs to determine the lowermost USDW (Table 1-14). The USDW base is then established at the base of the sand unit containing the lowermost USDW, if at least 100 feet of net shale exists between the USDW base and the next zone.

Table 1-14 – Depth and Resistivity Cutoffs for USDW Consideration

Depth (feet)	Resistivity (ohm-m)
0-1,000	3
1,000-2,000	2.5
2,000+	2

In the vicinity of the Hummingbird Project the base of USDW is contained within the Chicot, and Evangeline aquifers (Figure 1-43; Lindaman, 2023).

[redacted]

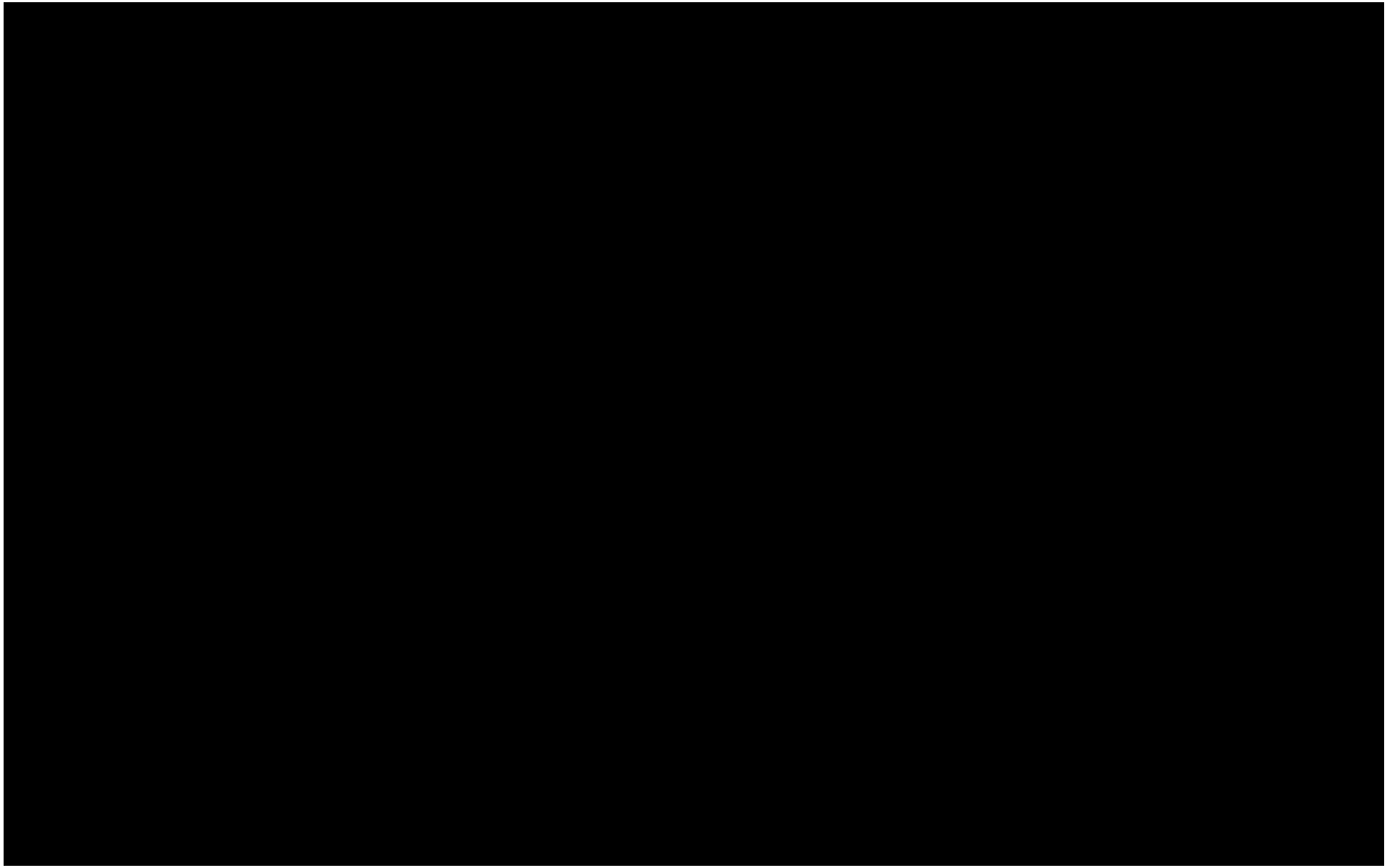

1.9 Site Evaluation of Mineral Resources

1.9.1 Active Mining Near the Proposed Injection Location

By referencing the USGS Mines and Quarries geodatabase, nearby mineral deposits were reviewed and mapped. A gravel/borrow pit to the [redacted]t of the AOR is the closest identified feature to the project. Further afield, numerous other sand and gravel pits dot the area along the [redacted] No surface mineral impacts from the Hummingbird Project will occur at the identified pits.

A separate search using public data provided by the USGS Mineral Resources Data System was also conducted. The primary features identified during this search were the Gulf Coast salt domes. [redacted] No impacts from the Hummingbird Project are expected to occur at these locations. [redacted]

[redacted]

1.9.2 Oil and Gas Resources

The first substantial exploration efforts for oil and gas in this part of Louisiana occurred in the 1950s, although available records show some wells possessing a spud date in the 1930s. Wells tend to follow the west-to-east trend of the Gulf Coast strata in this region. This is evident in Figure 1-50, where a couple banks of wells in the area migrate linearly north and south of the Hummingbird AOR. Within 5 miles of the centroid of the AOR, [redacted]

[redacted] All these wells, however, are plugged and abandoned, leaving offset production unaffected.

The minor historical production in the injection zone makes the area well suited for the injection and sequestration of CO_2. Any wellbores within the AOR that are drilled through the injection zone are discussed in *Section 3 – Area of Review and Corrective Action Plan*.

1.10 Seismic History

1.10.1 Historical Seismic Events

1.10.1.1 Seismic monitoring stations in and around Louisiana from All Relevant Databases

Multiple networks of seismic monitoring stations are deployed in and around Louisiana or have been deployed in the past for earthquake and microseismic monitoring, for research, by hobbyists, and for public use (Figure 1-51). Each network has dedicated webpages to share information; however, the **Incorporated Research Institutions for Seismology** (IRIS) consortium maintains a website compiling information from all networks (IRIS: Data Services).

- The United States (US) National Network consists of more than 100 currently active permanent stations located at approximately 186 mile spacing across the US. The two closest stations are in Nacogdoches, Texas (US_NATX) and in Vicksburg, Mississippi (US_VBMS) (US Array - Reference Network).
- The Transportable Array is a network of seismometers that have operated at temporary sites across the US. The array's deployment covered Louisiana in 2011 and 2012, [redacted] This station [redacted]) was active from February 11, 2011 to December 06, 2012 (ANSS Stations (usgs.gov)). However, this station was selected to become permanent as part of the Central and Eastern US network and returned to monitoring January 15, 2015 (see below).
- The Central and Eastern US network has seismometers distributed throughout the Central and Eastern US; one-quarter of these stations were initially operated within the Transportable Array Network and were selected to become permanent. The next closest station [redacted]; FDSN: N4: Central and Eastern US Network).
- The Texas Seismology Network is a network of 29 permanent seismometer stations and additional portable stations deployed throughout Texas. The station nearest to the [redacted]; Texas Seismological Network Earthquake Catalog (utexas.edu).
- The Arkansas Seismic Network is a network of permanent and temporary stations operated by the Arkansas Geological Survey. The station nearest to the Hummingbird Project is [redacted] FDSN: AG: Arkansas Seismic Network)
- US Geological Survey Network is a network of stations operated by the USGS Albuquerque Seismology Laboratory. The station nearest to Hummingbird Project [redacted] Albuquerque Seismological Laboratory | U.S. Geological Survey (usgs.gov)
- The Global Seismographic Network is a network of 152 seismometer stations deployed worldwide for the monitoring of earthquakes. The station nearest to the Hummingbird Project [redacted] Station IU HKT (usgs.gov).

- The Induced Seismic in Louisiana Network (ISLA) was in northwest Louisiana, operated by Tulane University and was active from 2019 to 2022. The station nearest to the Hummingbird Project [redacted]) ISLA – Investigation of Seismicity in Louisiana – EES Research (tulane.edu)
- NetQuakes is a USGS program that deploys dense networks of seismometers to urban environments. The station nearest to the Hummingbird Project is [redacted]; NetQuakes (usgs.gov))
- Raspberry Shake is a hobbyist "citizen scientist" network. The station nearest to Hummingbird Project [redacted]; Earthquake & Earth Monitoring Solutions | Raspberry Shake)

1.10.1.2 Characterization of Seismic Events

Southern Louisiana is a tectonically quiet region, with the USGS predicting the expected number of earthquakes in 10,000-year period to be fewer than six events with a 2% chance in 50 years of peak ground acceleration reaching 0.04–0.06 (Figure 1-54; USGS, 2023). The earthquake closest to the proposed AOR had a 3.8 magnitude and occurred on October 16, 1983, near Sulphur, Louisiana [redacted] miles from the Hummingbird Project area (Figure 1-52). No other earthquake in the USGS database had an epicenter 50 miles or closer to the proposed AOR. The absence of historical seismicity near the Hummingbird Project and the significant distance for historical seismic events supports that the likelihood of a seismic event within the proposed AOR is low. Information about ExxonMobil's site-specific response for seismic events can be found in the Emergency and Remedial Response Plan (see Section 8 Emergency and Remedial Response Plan).

[redacted]

1.10.2 Regional Faults and Project Influence

Sections 1.5.2 and *1.6* discuss regional faulting and stress conditions, respectively. Faults specific to the AOR are discussed in the following section.

1.10.3 Fault Slip Model

The injection pressures will be limited to values that reduce the potential for the initiation or propagation of fractures. No induced seismicity is expected to occur under the proposed permit conditions. The following evaluations were conducted to provide a site-specific technical evaluation of the seismic risk within the AOR.

[redacted] The fault slip potential was assessed using a deterministic 3D approach—based on an integrated pore-pressure prediction estimate of the stress gradients and the pore pressure increase at fault-formation interfaces. The modeled output is the approximated pore pressure needed for the fault to slip at each point on the fault. The estimates of the stresses included a vertical gradient of [redacted] with depth-dependent variations shown in Figure 1-33 (*Section 1.6.1.2*), and a pore pressure gradient of [redacted] The orientation of the maximum horizontal stress was taken from the World Stress Map, trending [redacted] to account for slight rotations of the stresses in Hummingbird Project area. The coefficient of friction used within the modeling is [redacted]

The amount of pore pressure required for fault slip is defined as the horizontal distance between the Mohr circle and the failure line. By constraining the stress state and pore pressure at each location along the fault, based on regional leak-off test data (Shmin) and the integration of the density log (Sv)—as well as the fault geometry (fault dip and fault strike)—the critical pore pressure for fault slip can be computed by assuming a friction coefficient for faults.

This methodology neglects poroelastic stresses due to the rock frame deformation and assumes that the regional stresses are representative of the stresses at the fault location. The resulting deterministic approach indicates that injection activities would have to increase pore pressures by more than [redacted] The current estimate of the maximum pore pressure increase anywhere in the injection zone, based on the simulation model, [redacted] indicating that the potential for induced seismic risk based on this methodology is low.

Figure 1-53 shows the estimated pore pressure increase required to induce fault slip along mapped faults most [redacted] The pore pressure increase along each fault trace is below the fault slip criterion. Fault traces are represented by spheres, colored by the pressure needed to induce reactivation.

Figure 1-54 shows a 3D representation of fault reactivation pressure along the surfaces of the faults

1.10.4 Seismic Hazard

Combined, the national seismic assessment, the absence of historical seismicity, and the analysis described in *Section 1.10.3* suggest that the potential for induced seismicity from CO_2 injection at the project area is not a significant risk.

Based on the seismic history of the Hummingbird Project area and the conforming pore pressure calculations, the potential for induced seismicity from CO_2 injection at the project area is not a significant risk.

1.11 Conclusion

The Hummingbird Project is a suitable location for CO_2 injection and storage operations. The upper confining zone (UCZ) and deeper, redundant intraformational seals: [redacted] are characterized by low porosity and permeability, modeled to impede upward migration of fluids—and will provide multiple seals of sufficient thickness and lateral continuity to protect USDW. The injection zone is sufficiently thick, porous, and

permeable to support the proposed injection operations. The lower confining zone provides thousands of feet of impermeable shale to contain injected fluids to the proposed injection zone. For the Hummingbird Project, critical favorable factors include:

- The area structure is well constrained by 3D seismic data and high-confidence well ties, indicating a low dip within the injection and confining system.
- Faults have been identified, characterized, and analyzed in the project area. [redacted] No other known conduits exist.
- Geomechanical properties and local stress conditions support the proposed Hummingbird Project operations.
- Baseline geochemistry and geochemical modeling of the in-situ fluid and injectate support the containment of injected fluids to the injection zone.
- Hydrologic units above the proposed injection zone are characterized and mapped. Risk to USDW by the Hummingbird Project's operations is low.
- Proposed operations will not affect active offset mineral resources.
- The Hummingbird Project is reported by the USGS to be characterized by very low seismic hazard.
- Fault slip potential was assessed, and no induced seismicity is expected to occur under the proposed operating conditions.

Data gathered from the proposed stratigraphic test well, [redacted] will be utilized in the verification of interpreted data and further characterization of the site-specific geology. The site geologic and hydrologic information presented herein were used to construct a 3D geomodel to simulate the plume and demonstrate the feasibility of the project (see *Section 2 Plume Model and Section 3 Area of Review).*

1.12 References

Allen, D.E., Strazisar, B.R., Soong, Y., and Hedges, S.W. (2005). Modeling carbon dioxide sequestration in saline aquifers: Significance of elevated pressures and salinities. *Fuel Processing Technology* 86, 1569-1580.

Albuquerque Seismological Laboratory | U.S. Geological Survey. (n.d.). https://www.usgs.gov/centers/geologic-hazards-science-center/albuquerque-seismological-laboratoryAngel, M., Jr. and Whiteman, C.D., Jr. (1985). Generalized potentiometric surface of the Evangeline and equivalent aquifers in Louisiana, 1980, Water-Resources Investigations Report 84-4359, https://doi.org/10.3133/wri844359

ANSS Stations. (n.d.). https://earthquake.usgs.gov/monitoring/operations/network.php?virtual_network=ANSS

Baker, E.T., Jr. (1979). Stratigraphic and hydrogeologic framework of part of the Coastal Plain of Texas: Texas Dept. Water Resources Rept. 236, 43 p.

Best, M.G., and Grant, S.K. (1987). Oligocene and Miocene Volcanic Rocks in the Central Pioche-Marysvale Igneous Belt, Western Utah and Eastern Navada. U.S. Geological Survey Professional Paper 1433.

Bethke, C.M. (2022). Geochemical and biogeochemical reaction modeling 3rd edition. Cambridge University Press.

Bethke, C.M., Farrell, B. and Yeakel, S. (2022). The Geochemist's Workbench (Version 12.0): Reaction modeling guide. Aqueous Solutions, LLC, Champaign, Illinois.

Bird, D.E., Burke, K., Hall, S.A., and Casey, J.F. (2005). Gulf of Mexico tectonic history: hotspot tracks, crustal boundaries, and early salt distribution. *AAPG Bulletin*, Vol. 89, 311–328.

Blondes, M.S., Knierim, K.J., Croke, M.R. et al. (2023). U.S. Geological Survey National Produced Waters Geochemical Database (Version 3.0, November 2023).

Brantley, S.L. (1992). Kinetics of dissolution and precipitation – experimental and field results. In Y.K. Kharaka and A.S. Maest (eds.), *Water-Rock Interaction.* Balkema, Rotterdam, 3-6.

Bruun, B., Anaya, R., Boghici, R. et al. (2016). Texas Aquifers Study: Chapter 6, Gulf Coast Aquifers. In: Texas Aquifers Study, Groundwater Quantity, Quality, Flow, and Contributions to Surface Water: Texas Water Development Board Report.

Chowdhury, A.H., Boghici, R., and Hopkins, J. (2006). Hydrochemistry, Salinity Distribution, and Trace Constituents: Implications for Salinity Sources, Geochemical Evolution, and Flor

Systems Characterization, Gulf Coast Aquifer, Texas. Chapter 5 in: Mace, R.E. et al. (eds.), Aquifers of the Gulf Coast of Texas: Texas Water Development Board Report.

Chowdhury, A.H., and Turco, M.J. (2006). Geology of the Gulf Coast Aquifer, Texas. Chapter 2 in: Mace, R.E. et al. (eds.), Aquifers of the Gulf Coast of Texas: Texas Water Development Board Report.

Davidson, S.C., and Mace, R.E. (2006). Aquifers of the Gulf Coast of Texas: An Overview. Chapter 1 in: Mace, R.E. et al. (eds.), Aquifers of the Gulf Coast of Texas: Texas Water Development Board Report.

Duan, Z., and Sun, R. (2003). An improved model calculating CO_2 solubility in pure water and aqueous NaCl solutions from 273 to 533 K and from 0 to 2000 bar. *Chemical Geology* 193, 257-271.

Earthquake & Earth Monitoring Solutions | Raspberry Shake. (n.d.). Raspberry Shake. https://raspberryshake.org/

FDSN: AG: Arkansas Seismic Network. (n.d.). https://www.fdsn.org/networks/detail/AG/

FDSN: N4: Central and Eastern US Network. (n.d.). http://www.fdsn.org/networks/detail/N4/

Galloway, W.E. (2008). Depositional Evolution of the Gulf of Mexico Sedimentary Basin, in Miall, A.D. (ed.), Sedimentary Basins of the World, Vol. 5, 505-549.

Galloway, W.E., Whiteaker, T. L., and Ganey-Curry, P. (2011). History of Cenozoic North America drainage basin evolution, sediment yield, and accumulation in the Gulf of Mexico basin. *Geosphere*, Vol. 7, No. 4, 938-973.

Gaus, I. (2010). Role and impact of CO_2–rock interactions during CO_2 storage in sedimentary rocks. *International Journal of Greenhouse Gas Control* 4, 73–89.

Gherardi, F., Xu, T., and Pruess, K. (2007). Numerical modeling of self-limiting and self-enhancing caprock alteration induced by CO_2 storage in a depleted gas reservoir. *Chemical Geology* 244 (1), 103-129.

Gray, G.G., Pottorf, R.J., Yurewicz, D.A. et al. (2001). Thermal and chronological record of syn- to post- Laramide burial and exhumation, Sierra Madre Oriental, Mexico. In: Bartolini, C., Buffler, R.T., and Cantú-Chapa, A. (eds.), The Western Gulf of Mexico Basin: Tectonics, Sedimentary Basins, and Petroleum System.

Hanor, J. S. (1982). Reactivation of fault movement, Tepetate fault zone, south central Louisiana. Gulf Coast Association of Geological Societies *Transactions*, Vol. 32, 237-245.

Haq, B.U., Hardenbol, J., and Vail, P.R. (1988). Mesozoic and Cenozoic Chronostratigraphy and Cycles of Sea-Level Change. In: Wilgus, C.K. et al. (eds.), Sea-Level Changes: An Integrated Approach, SEPM Special Publication 42, 71-108.

IRIS: Data Services. (n.d.). https://ds.iris.edu/ds/

ISLA – Investigation of Seismicity in Louisiana – EES Research. (n.d.). https://ebinger.wp.tulane.edu/research/isla/

Jacques, J. M., and Clegg, H. (2002). Late Jurassic source rock distribution and quality in the Gulf of Mexico: inferences from plate tectonic modeling. Gulf Coast Association of Geological Societies Transactions, Vol. 52, 429–440.

Lindaman, M.A. (2023). Hydrogeologic framework of southwestern Louisiana: U.S. Geological Survey Scientific Investigations Report 2023–5004, 31 p., https://doi.org/10.3133/sir20235004

Lovelace, J., Fontenot, J., and Frederick, C. (2002). Louisiana Ground-Water Map No. 14, U.S. Geological Survey.

Lundstern, J.E., and Zoback, M.D. (2020). Multiscale variations of the crustal stress field throughout North America. *Nat Commun* 11, 1951 (2020). https://doi.org/10.1038/s41467-020-15841-5

Manzocchi, T., Walsh, J.J., Nell, P., and Yielding, G. (1999). Fault transmissibility multipliers for flow simulation models. *Petroleum Geoscience* Vol. 5, European Association of Geoscientists and Engineers, 53-63.

Martin, A., and Whiteman, C.D. (1985). Generalized Potentiometric Surface of the Evangeline and Equivalent Aquifers in Louisiana, 1980. USGS Water Resources Investigation Report 87-4359. https://pubs.usgs.gov/wri/1984/4359/plate-1.pdf

NetQuakes. (n.d.). https://earthquake.usgs.gov/monitoring/netquakes

Palandri, J.L., and Kharaka, Y.K. (2004). A compilation of rate parameters of water-mineral interaction kinetics for application to geochemical modeling. USGS Open File Report 2004-1068, 64 p.

Prakken, L.B., Griffith, J.M., and Fendick, R.B., Jr. (2012). Water resources of Allen Parish: U.S. Geological Survey Fact Sheet 2012–3064, 6 p., https://doi.org/10.3133/fs20123064

Raymer, L., Hunt, E. and Gardner, J.S. (1980). An Improved Sonic Transit Time-to-Porosity Transform. Proceedings of Society of Petrophysicists and Well-Log Analysts, Houston, 1-13.

Texas Seismological Network Earthquake Catalog. (n.d.). https://www.beg.utexas.edu/texnet-cisr/texnet/earthquake-catalog

Salvador, A. (1987). Late Triassic-Jurassic paleogeography and origin of Gulf of Mexico basin. *AAPG Bulletin*, Vol. 71, 419–451.

Sawyer, D.S., Buffler, R.T., and Pilger Jr., R.H. (1991). The crust under the Gulf of Mexico Basin. In: A. Salvador (ed.), The Gulf of Mexico Basin: The Geology of North America: Geological Society of America, 53–72, doi:10.1130/ DNAG-GNA-J.53s: American Association of Petroleum Geologists, Memoir 75, 159–181.

Seismic Information. (n.d.). CERI - the University of Memphis. https://www.memphis.edu/ceri/seismic/

Seismology, I.-. I. R. I. F. (n.d.). *USArray - Reference Network*. IRIS - Incorporated Research Institutions for Seismology. http://www.usarray.org/researchers/obs/reference

Shiraki, R., and Dunn, T.L. (2000). Experimental study on water–rock interactions during CO_2 flooding in the Tensleep Formation, Wyoming, USA. *Applied Geochemistry* 15, 265–279.

Sperrevik, S., Gillespie, P.A., Fisher, Q.J. et al. (2002). Empirical estimation of fault rock properties, Hydrocarbon Seal Quantification. Norwegian Petroleum Society Special Publication Vol. 11, 109-125.

Station IU HKT. (n.d.). https://earthquake.usgs.gov/monitoring/operations/stations/IU/HKT/

Strategic Online Natural Resources Information System (SONRIS) online database and GIS mapping tool; https://www.sonris.com/

Tang, Y., Hu, S., He, Y. et al. (2021). Experiment on CO_2-brine-rock interaction during CO_2 injection and storage in gas reservoirs with aquifer. *Journal of Chemical Engineering* 413, 127567.

Thorkildsen, D., and Quincy, R. (1990). Evaluation of Water Resources of Orange and Eastern Jefferson Counties, Texas: Texas Water Development Board Report 320.

U.S. Geological Survey (2023). 2023 US 50-State Long-term National Seismic Hazard Map. https://www.usgs.gov/programs/earthquake-hazards/science/2023-50-state-long-term-national-seismic-hazard-model

Warick, P.D., and Corum, M.D. (eds.) (2012). Geologic framework for the national assessment of carbon dioxide storage resources. U.S. Geological Survey Open-File Report 2012-1024.

Winker, C.D., and Buffler, R.T. (1988). Paleogeographic evolution of early deep-water Gulf of Mexico and margins, Jurassic to Middle Cretaceous (Comanchean). *AAPG Bulletin*, Vol. 72, 318–346.

Wolery, T.J. (1992). EQ3/EQ6, A software package for geochemical modeling of aqueous systems: package overview and installation guide (Version 7). Lawrence Livermore National Laboratory Report, UCRL-MA-110662, 66 p.

Xu, T., Sonnenthal, E., Spycher, N. and Pruess, K. (2006). TOUGHREACT – A simulation program for non-isothermal multiphase reactive geochemical transport in variably saturated geologic media: Applications to geothermal injectivity and CO_2 geological sequestration. *Computers & Geosciences* 32, 145-165.

Xu, T., Zhend, L., and Tian, H. (2011). Reactive transport modeling for CO_2 geological sequestration. *Journal of Petroleum Science and Engineering* 78, 765-777.

Yielding, G., Freeman, B., and Needham, D.T. (1997). Quantitative fault seal prediction, *AAPG Bulletin*, Vol. 81 (6), 897-917.

Young, S.C. et al. (2016). FINAL REPORT: Identification of Potential Brackish Groundwater Production Areas - Gulf Coast Aquifer System. Prepared by INTERA Inc. for Texas Water Development Board, Contract Report Number 1600011947.

Zerai, B., Saylor, B.Z., and Matisoff, G. (2006). Computer simulation of Co2 trapped through mineral precipitation in the Rose Run Sandstone, Ohio. *Applied Geochemistry* 21 (2), 223-240.

Appendix B – Site Characterization